Check for updates

ADVANCING EARTH AND SPACE SCIENCES

JGR Solid Earth

RESEARCH ARTICLE

10.1029/2024JB029961

Softening and Recovery of Near-Surface Layers During the 2024 M7.6 Noto Earthquake

Miroslav Hallo[1], **Kimiyuki Asano**[1], **and Tomotaka Iwata**[2]

[1]Disaster Prevention Research Institute, Kyoto University, Uji, Japan, [2]Professor Emeritus, Kyoto University, Kyoto, Japan

Key Points:

- Analysis of Horizontal-to-Vertical spectral ratios from earthquake waveforms recorded at 160 sites in the years 1996–2024
- The 2024 M_J 7.6 Noto Peninsula earthquake caused short- and long-lasting site-response changes at strongly shaking sites
- The temporal changes can be attributed to elastic softening and subsequent recovery of near-surface geological layers

Supporting Information:

Supporting Information may be found in the online version of this article.

Correspondence to:

M. Hallo,
hallo.miroslav.46v@st.kyoto-u.ac.jp

Citation:

Hallo, M., Asano, K., & Iwata, T. (2025). Softening and recovery of near-surface layers during the 2024 M7.6 Noto earthquake. *Journal of Geophysical Research: Solid Earth*, *130*, e2024JB029961. https://doi.org/10.1029/2024JB029961

Received 19 JUL 2024
Accepted 28 MAR 2025

Author Contributions:

Conceptualization: Miroslav Hallo
Data curation: Miroslav Hallo, Kimiyuki Asano, Tomotaka Iwata
Formal analysis: Miroslav Hallo
Funding acquisition: Kimiyuki Asano
Investigation: Miroslav Hallo, Kimiyuki Asano, Tomotaka Iwata
Methodology: Miroslav Hallo
Project administration: Kimiyuki Asano
Resources: Miroslav Hallo, Kimiyuki Asano, Tomotaka Iwata
Software: Miroslav Hallo
Supervision: Kimiyuki Asano, Tomotaka Iwata
Validation: Miroslav Hallo
Visualization: Miroslav Hallo
Writing – original draft: Miroslav Hallo

© 2025. The Author(s).
This is an open access article under the terms of the Creative Commons Attribution License, which permits use, distribution and reproduction in any medium, provided the original work is properly cited.

Abstract On 1 January 2024, a devastating M_J 7.6 earthquake occurred on the Noto Peninsula in Japan. When such a strong earthquake occurs, affected near-surface soil layers behave nonlinearly and may undergo some structural changes driven by Flow Liquefaction, Cyclic Mobility, or Slow Dynamics phenomena. The structural changes can be manifested by short-lasting coseismic and long-lasting postseismic site-response changes that are related to variations in near-surface shear-wave velocity. To examine this behavior, we perform a systematic analysis of Horizontal-to-Vertical (H/V) spectral ratios from regional earthquake waveforms recorded at 160 sites in the years 1996–2024. We identify significant H/V peaks and their directionality in the frequency range of 0.1–25 Hz separately for periods before and after the M_J 7.6 earthquake. This allows us to measure long-lasting relative changes in predominant frequency caused by the strong shaking, with maximum drops of −21% and a dependence on experienced ground motion levels. Next, the short-lasting changes during the M_J 7.6 earthquake reveal strongly nonstationary behavior. The frequency of spectral peaks decreases simultaneously and omnidirectionally with the strong shaking and then logarithmically recovers. The observed extreme short-lasting predominant frequency drops reach −93% relative to the initial value, and their occurrence time divides the nonstationary behavior into elastic softening and recovery phases. This behavior is physically related to temporal changes in near-surface shear-wave velocity as a consequence of changes in shear moduli. The introduced phenomenon of elastic softening and recovery may have a significant impact on a broad scale of geophysical research topics.

Plain Language Summary When a strong earthquake strikes, the shaking causes changes in the physical properties of the affected material near the surface. You can think of it like sprinkling buns with sugar through a sieve. If you shake the sieve, the sugar will fall smoothly onto the buns. If you stop shaking, the sugar will not fall as easily. Although the physical principle is different, earthquake shaking causes a softening of near-surface soils and rocks that may be observed by geophysical methods. Here, we observe and quantitatively evaluate this softening and subsequent recovery during and after the 2024 earthquake that occurred on the Noto Peninsula in Japan. This is a unique and complex study with a potentially wide scientific impact.

1. Introduction

On 1 January 2024 at 16:10 (Japan Standard Time), a devastating earthquake occurred on the Noto Peninsula in Ishikawa Prefecture of Japan. The earthquake and accompanying tsunami caused more than 462 confirmed deaths, collapses of houses, widespread damage to civil infrastructure, and crustal uplift of up to 4 m (Fujii & Satake, 2024). Strong ground shaking and building damage were observed also in neighboring Toyama and Niigata Prefectures. The Japan Meteorological Agency (JMA) evaluated the magnitude to be M_J 7.6 (JMA magnitude scale) and reported a maximum seismic intensity of 7 (Shindo 7) which is the highest level of the JMA seismic intensity scale. The JMA hypocenter is located under the northeastern tip of the Noto Peninsula at a depth of 16 km and the source fault has a NE–SW-striking reverse faulting plane. According to Asano and Iwata (2024), the source process consists of two almost equally sized subevents that occurred on several reverse faults. First, the rupture propagated from the hypocenter to the SW direction beneath the Noto Peninsula; 13 s later, the rupture extended to offshore fault segments in the NE direction.

The regional tectonics is dominated by the NW–SE compression regime (Terakawa & Matsu'ura, 2010) that has been active since the late Pliocene. In the last decades, large earthquakes occurred in the region on 7 February 1993 (M_J 6.6), 25 March 2007 (M_J 6.9; Asano & Iwata, 2011; Kurahashi et al., 2008; Sakai et al., 2008), 5 May 2023 (M_J 6.5; Kato, 2024), and 1 January 2024 (M_J 7.6). Moreover, since November 2020, the northeastern tip of the Noto Peninsula has hosted an intensive earthquake swarm that is driven by an upward flow of pressurized

Writing – review & editing: Kimiyuki Asano, Tomotaka Iwata

fluids along crustal faults from the uppermost mantle (Amezawa et al., 2023; Nakajima, 2022; Nishimura et al., 2023; Yoshida et al., 2023). Most earthquake sources have shallow crustal hypocenters and reverse faulting mechanisms along NE–SW-striking faults. Ohmi et al. (2008) found a sudden change in the lag time of the autocorrelation function of seismic noise at regional seismic stations, which is associated with the occurrence of the 2007 M_J 6.9 earthquake. This is interpreted as a temporal decrease of seismic velocities. Effects of near-surface layers (i.e., site response) were investigated by Yoshimi and Yoshida (2008) and Asano et al. (2009), who found that these effects are spatially variable and play an important role on the Noto Peninsula. Further, Iwata et al. (2008) investigated temporal variations of Horizontal-to-Vertical (H/V) spectral ratios of observed strong motions at the station ISK005 for the 2007 M_J 6.9 earthquake. They observed a short-lasting decrease of the H/V peak frequency that recovered within approximately 10 s and it was interpreted as the nonlinear soil response.

A common method to evaluate the site response is the spectral ratio technique by Borcherdt (1970); nevertheless, it requires a reference seismic station. For only one station, the characterization of the site response can be performed using the spectral ratio between Horizontal and Vertical components of motion (H/V spectral ratio) either from ambient vibrations (Nakamura, 1989; Nogoshi & Igarashi, 1971) or regional earthquakes (Lermo & Chávez-García, 1993). According to Nakamura (2000), the H/V spectral peaks may represent the first-order proper frequency due to multiple reflections of *SH* waves (horizontally polarized shear waves) in the near-surface soil layer. Other studies showed that observed H/V ratios include contributions from Rayleigh waves (Fäh et al., 2001) and Love waves (Bonnefoy-Claudet et al., 2008). In reality, the observed wavefield and H/V ratios are the results of a mix of several types of waves; hence, numerical modeling studies usually propose a separation of body and surface waves, as is done by the diffuse field theory (Sánchez-Sesma et al., 2011), the random decrement technique (Hobiger et al., 2009), or the wavefield decomposition method (Maranò et al., 2012). When considering a mixed wavefield, the energy flux ratio of body and surface waves influences primarily amplitudes of H/V peaks, while their frequencies are rather stable (e.g., Bonilla et al., 1997; Parolai et al., 2004). Further, the ambient vibration wavefield can include a high amount of surface waves because microtremor sources are located at the ground surface, while the regional earthquake wavefield consists predominantly of body waves (e.g., Kawase et al., 2018). In this paper, we use H/V spectral ratios computed from regional earthquakes only and we focus on the frequency (not amplitude) of H/V peaks; hence, we mainly investigate site-response characteristics of incident body waves.

The site response has its origin in the material properties of near-surface layers (e.g., Kramer, 1996). The most important is the shear wave (*S*-wave) velocity V_S as a function of depth. The near-surface *S*-wave velocity influences wave amplitudes, and the stratigraphic interfaces with high impedance contrasts cause spectral resonance peaks. The site response is linear if ground motions cause only small elastic deformations in the rock and soil materials. When strong ground motions occur, the soil behavior is nonlinear in the stress-strain space and shows hysteresis (e.g., Aguirre & Irikura, 1997; Assimaki et al., 2008; Beresnev & Wen, 1996; Kawase et al., 1995; Régnier et al., 2013; Sato et al., 1996), and a short-lasting degradation of shear moduli of soils may occur (Pavlenko & Irikura, 2006). Note, that the shear moduli degradation causes a short-lasting reduction of the *S*-wave velocity of near-surface layers. Further, under some special conditions, the near-surface layers may undergo structural changes driven by:

- *Flow Liquefaction* is a commonly observed phenomenon (Castro, 1975; Nagase & Ishihara, 1988; Seed & Idriss, 1967). It occurs in loose sandy saturated soils, in which a shaking-generated increase of pore pressure exceeds contact stresses between grains and causes a loose of the shear strength and stiffness. After the shaking, the sandy soil is compacted.
- *Cyclic Mobility* can occur in any type of soil and even in dense ones (Castro, 1975; Iai et al., 1995). In this case, the strong shaking causes a decrease in pore pressure; hence, the shear strength remains greater than the static shear stress, and the shear resistance increases. After the shaking, the soil has increased volume, which can gradually subside in the long term.
- *Slow Dynamics* is a known physical property of geomaterials (Guyer et al., 1998; Scalerandi et al., 2010; TenCate et al., 2000; TenCate & Shankland, 1996), but until now, it has been almost ignored in earthquake science. We recommend considering it because it can explain long-lasting *S*-wave velocity changes in rock formations after a strong shaking. Any material, including iron, hard rock, or cemented soils, rapidly degrades its elastic moduli when exposed to strong cyclic shaking. This is due to a loss of microscopic contact area between grains to minimize free energy in the material. Such a reduction of elastic moduli and pressure wave velocity accompanied by an increase in the medium damping was empirically observed in laboratory

21699356, 2025, 4, Downloaded from https://agupubs.onlinelibrary.wiley.com/doi/10.1029/2024JB029961 by Cochrane Japan, Wiley Online Library on [03/06/2025]. See the Terms and Conditions (https://onlinelibrary.wiley.com/terms-and-conditions) on Wiley Online Library for rules of use; OA articles are governed by the applicable Creative Commons License

10.1029/2024JB029961

experiments (Ostrovsky et al., 2019; Shokouhi et al., 2017). Importantly, the elastic moduli do not recover immediately after the end of the shaking, but they recover gradually in the long term following a logarithmic curve. These effects were observed from both the fault zone (Li et al., 1998) and strongly shaking near-surface layers (Rubinstein et al., 2007; Schaff & Beroza, 2004).

The short- and long-lasting site-response changes generated by strong ground motions have been identified in Surface-to-Borehole (S/B) spectral ratios from boreholes in the past. In particular, Sawazaki et al. (2006) observed drops in the predominant resonant frequency of S/B spectral ratios at three sites during the 2000 M_w 6.7 Tottori and the 2003 M_w 8.3 Tokachi-Oki earthquakes in Japan. The maximal reduction of the predominant frequency reached 30%–70%, and then, logarithmically recovered to values before the strong shaking (long-lasting recovery of a few tens of minutes to several years). Wu and Peng (2011, 2012) analyzed short-lasting and long-lasting temporal changes in S/B ratios at six sites during the 2011 M_w 9.0 Tohoku earthquake in Japan. Their results show a clear drop of the predominant resonant frequency by 70% followed by logarithmic recovery. Next, Sawazaki et al. (2009) performed the Surface-Borehole deconvolution to investigate long-lasting changes in shear moduli and *S*-wave velocities after the 2000 M_w 6.7 Tottori earthquake. Their analysis indicates the same pattern of temporal changes in *S*-wave velocity and predominant frequency (estimated affected depth of 0–11 m). Further, Bonilla et al. (2019) performed the Surface-Borehole autocorrelation analysis at one borehole site. They concluded that the near-surface *S*-wave velocity dropped suddenly by 60% during the 2011 M_w 9.0 Tohoku earthquake and then gradually recovered (the estimated affected depth is the first tens of meters). Nevertheless, these studies have been performed at a very limited number of sites and require data from borehole seismic arrays. As concluded by Wen et al. (2006), the H/V ratios of surface records can be used for the identification of nonlinear site responses during strong shaking. Still, we are aware of only one analysis of temporal changes in H/V ratios generated by strong ground motions by Vassallo et al. (2022). They found 10% drop in the dominant H/V frequency followed by logarithmic recovery. In addition, the site-response changes can be also caused by the shaking from a buried chemical explosion (Viens & Delbridge, 2024).

In this research, we perform a systematic analysis of H/V spectral ratios from regional earthquake waveforms recorded at 160 sites of the Noto Peninsula and its surrounding region in the years 1996–2024. We identify H/V spectral peaks originating from stratigraphic interfaces of various depths including their predominant directionality. Then, we evaluate the long-lasting changes in site response caused by the 2024 M_J 7.6 Noto Peninsula earthquake using a comparison of predominant frequencies before and after the earthquake. The short-lasting coseismic changes during the M_J 7.6 Noto earthquake are assessed by using a short-time Fourier transform, and sites with identified strongly nonstationary behavior are investigated in detail. The validation of temporal changes in H/V spectral ratios is performed by comparison with changes in S/B ratios at borehole sites. Next, to investigate the physical cause behind this phenomenon, we model the theoretical site response at selected sites and the effects of the *S*-wave velocity change in multilayer structure. As a result, this research is a unique and complex analysis of elastic softening and subsequent recovery of near-surface layers during the 2024 M_J 7.6 Noto Peninsula earthquake.

2. Earthquake Waveforms

This study is based on earthquake waveforms that were recorded by strong-motion monitoring networks at 160 regional sites in the period 1996–2024. The investigated region includes Ishikawa and Toyama Prefectures in Japan, which were the most affected by the 2024 M_J 7.6 Noto Peninsula earthquake. The map of seismic stations used in this study is shown in Figure 1. The waveform data originate from various monitoring networks as follows.

- The K-NET and KiK-net strong-motion seismogram networks (Kyoshin and Kiban Kyoshin Network, respectively) are operated by the National Research Institute for Earth Science and Disaster Resilience (NIED; Aoi et al., 2020; National Research Institute for Earth Science and Disaster Resilience, 2019). K-NET stations have a three-component strong-motion sensor deployed on the ground surface, while KiK-net stations consist of pairs of seismometers installed on the surface and in a borehole.
- The Japan Meteorological Agency (JMA) is operating the national-wide seismic intensity monitoring network Shindo-kei. Despite different purposes, the seismic intensity meters are capable of recording and preserving strong ground-motion waveforms because the used sensors are three-component accelerometers (Nishimae, 2004).

21699356, 2025, 4, Downloaded from https://agupubs.onlinelibrary.wiley.com/doi/10.1029/2024JB029961 by Cochrane Japan, Wiley Online Library on [03/06/2025]. See the Terms and Conditions (https://onlinelibrary.wiley.com/terms-and-conditions) on Wiley Online Library for rules of use; OA articles are governed by the applicable Creative Commons License

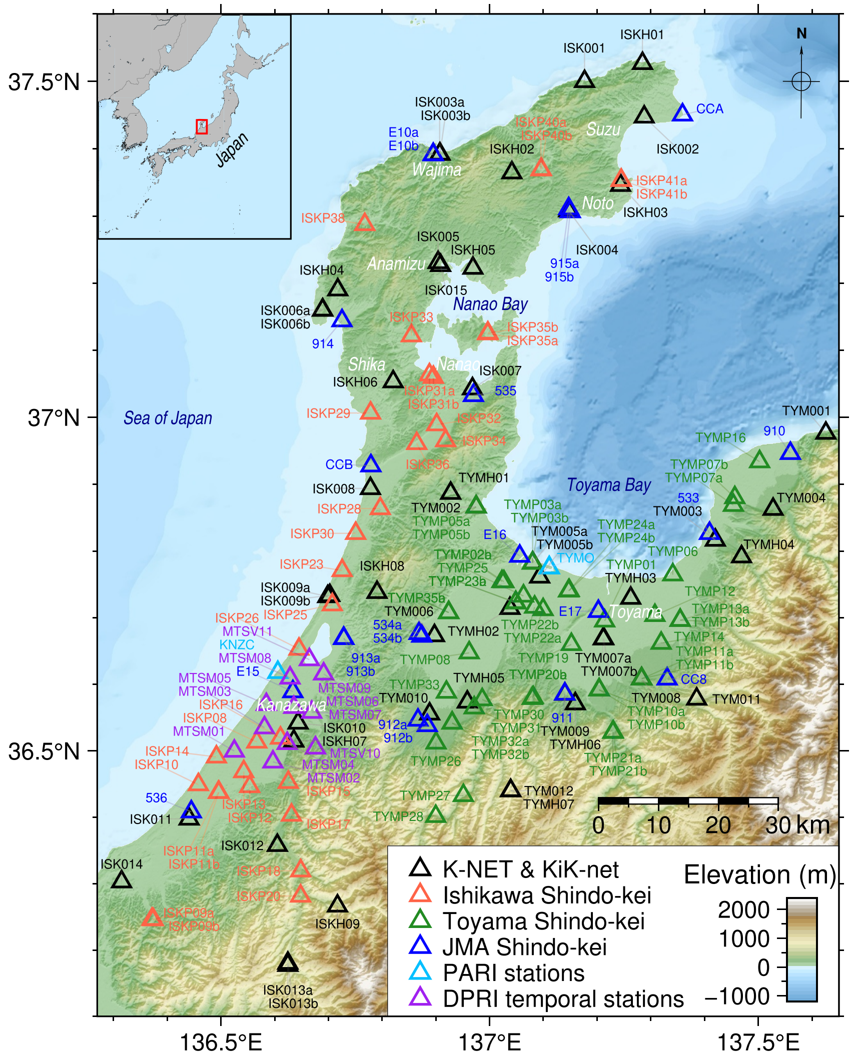

Figure 1. Map of the Noto Peninsula in Japan with locations of strong-motion monitoring stations. Seismic sensors are located in the centers of displayed triangles. Monitoring station operators are distinguished by color (see legend). The inset in the top left corner shows the location within Japan (by red rectangle).

- The Ishikawa and Toyama Prefectural Shindo-kei networks are operated by local governments for seismic intensity monitoring purposes. Similarly to the JMA Shindo-kei, the Prefectural Shindo-kei networks are capable of preserving three-component strong ground-motion waveforms (Nishimae, 2004).
- The strong-motion earthquake observation in Japanese Ports has been conducted by the Port and Airport Research Institute (PARI) since 1962. After the modernization in past decades, it is conducted by modern three-component accelerometers (Nozu, 2004).
- The temporal earthquake monitoring around the Morimoto-Togashi Fault Zone (Kanazawa and Hakusan Cities) has been conducted by the Disaster Prevention Research Institute (DPRI) of Kyoto University from 2022 to 2025. The monitoring was a part of the comprehensive research project with the Headquarters for Earthquake Research Promotion.

Each seismic station is assigned a unique code (see Table 1). Some stations were relocated within the monitoring period by tens-to-thousand meters to a new location, which may have different site-response characteristics. To take this into account, we treat the relocated stations as separate sites in our analysis. Then, the station code ends with an additional lowercase letter (a—original site, b—relocated site). The waveforms are three-component acceleration time series of regional earthquakes with detectable levels of ground motion (see the waveform

21699356, 2025, 4, Downloaded from https://agupubs.onlinelibrary.wiley.com/doi/10.1029/2024JB029961 by Cochrane Japan, Wiley Online Library on [03/06/2025]. See the Terms and Conditions (https://onlinelibrary.wiley.com/terms-and-conditions) on Wiley Online Library for rules of use; OA articles are governed by the applicable Creative Commons License

21699356, 2025, 4, Downloaded from https://agupubs.onlinelibrary.wiley.com/doi/10.1029/2024JB029961 by Cochrane Japan, Wiley Online Library on [03/06/2025]. See the Terms and Conditions (https://onlinelibrary.wiley.com/terms-and-conditions) on Wiley Online Library for rules of use; OA articles are governed by the applicable Creative Commons License

Table 1
List of Strong-Motion Monitoring Networks

Network	Code[a]	Count of sites[b]	Data period[c]	Count of waveforms[d]
All	-	160	1996–2024	29,140
K-NET	ISK0·· and TYM0··	33	1996–2024	6,967
KiK-net	ISKH·· and TYMH··	16	1999–2024	10,302
JMA Shindo-kei	JMA### or ###	23	1997–2024	2,816
Ishikawa Shindo-kei	ISKP··	33	2010–2024	1,951
Toyama Shindo-kei	TYMP··	42	2010–2024	4,164
PARI stations	P_∗∗∗∗ or ∗∗∗∗	2	2013–2024	286
DPRI stations	MTSM·· and MTSV··	11	2022–2024	2,654

[a]The middle dot · substitutes a single-digit decimal number (0–9), # represents a single-digit hexadecimal number (0–F), and ∗ is one uppercase alphabet letter (A–Z). [b]Relocated stations are counted as separate sites. [c]The data period may be shorter than the operation period. [d]The count of all processed three-component earthquake waveforms.

count in Table 1, and Figures S1 and S2 in Supporting Information S1). They have a common sampling rate of 100 Hz (or 200 Hz for some distant-past events) and a length of 60–450 s (some longer records also exist).

3. Methods

3.1. H/V Earthquake Spectral Ratios

Let us assume one observation point on the ground surface (depth = 0). At this point, the three-dimensional ground acceleration during an earthquake can be described by three time series in orthogonal directions; two horizontal $x(t,0)$ and $y(t,0)$, and one vertical $z(t,0)$, where t is time. Horizontal components can be defined by cardinal directions (N–S, E–W, NE–SW, and SE–NW) or the back azimuth to the earthquake epicenter (Transverse and Radial components). The Fourier transform of these time series yields complex spectral functions $X(f,0)$, $Y(f,0)$, and $Z(f,0)$, where f is frequency. Then, the H/V spectral ratio $R_X(f)$ is expressed as

$$R_X(f) = \frac{|X(f,0)|}{|Z(f,0)|}, \tag{1}$$

in which $|\cdot|$ denotes absolute value and the index notation distinguishes horizontal directions. The formula for the H/V spectral ratio in the perpendicular horizontal direction, that is, $R_Y(f)$, is expressed by substituting $Y(f,0)$ for $X(f,0)$ in Equation 1.

Equation 1 expresses the H/V spectral ratio for a single earthquake. Practically, it is influenced by many event-specific features such as the incident wave angle at the depth of local bedrock, the ratio between horizontal and vertical spectral amplitudes of the incident wave, the ratio between the power of the body and Rayleigh waves on the ground surface, the back azimuth to the earthquake epicenter, and the seismic noise level during the earthquake. Hence, site-specific H/V spectral ratios (related to the linear site response) should be statistically evaluated from several moderate earthquakes, characterized by various source-site distances, back azimuths, and magnitudes. This multi-event H/V spectral ratio can be generally expressed by

$$\tilde{R}_X(f) = \mathbb{E}[R_X(f)], \tag{2}$$

in which $\mathbb{E}[\cdot]$ denotes the expectancy and the formula for the perpendicular horizontal direction $\tilde{R}_Y(f)$ is straightforward. To evaluate the expectancy, spectral curves of individual earthquakes are smoothed by the Konno-Ohmachi window with parameter $b = 40$ (Konno & Ohmachi, 1998). Also, spectral curves have evaluated their useful frequency range in which spectral amplitudes are at least three times larger than the noise ones. The noise spectra are event- and site-specific and computed from the time series foregoing the first wave arrival. Then, the multi-event H/V spectral ratio is defined as a median value from all useful spectra at the given frequency, and

21699356, 2025, 4, Downloaded from https://agupubs.onlinelibrary.wiley.com/doi/10.1029/2024JB029961 by Cochrane Japan, Wiley Online Library on [03/06/2025]. See the Terms and Conditions (https://onlinelibrary.wiley.com/terms-and-conditions) on Wiley Online Library for rules of use; OA articles are governed by the applicable Creative Commons License

it is supplemented with 16th and 84th percentiles capturing the inter-event variability. The H/V spectral ratios $\tilde{R}_X(f)$ and $\tilde{R}_Y(f)$ are statistically representative and related to the site-specific linear response.

3.2. Directionality of H/V Peaks

In the formulation by Equations 1 and 2, H/V spectral ratios are defined for two perpendicular horizontal directions. This definition allows us to evaluate the magnitude and azimuth of the predominant H/V peak directionality (see Text S1 and Figures S3 and S4 in Supporting Information S1). The H/V peak directionality allows for the discrimination between one-dimensional (1D) and other (2D/3D) resonance patterns. First, let us assume a H/V spectral peak defined by frequency f_l, where l is an index of the peak (e.g., f_0, f_1, f_2). Note that the index does not indicate the resonance mode. Because H/V spectral peaks have a non-zero bandwidth, we define cutoff frequencies $f_A\left(f_l\right)$ and $f_B\left(f_l\right)$ around the peak frequency as

$$f_A\left(f_l\right) = f_l/(1+\varepsilon) \text{ and} \tag{3}$$

$$f_B\left(f_l\right) = f_l \times (1+\varepsilon), \tag{4}$$

in which ε is a unitless parameter larger than zero; we use $\varepsilon = 0.16$. Then, following Matsushima et al. (2017), the magnitude of the directionality can be expressed by the directional dependency factor γ as

$$\gamma_{XY}\left(f_l\right) = \frac{1}{n}\sum_{f=f_A(f_l)}^{f_B(f_l)} \sqrt{\frac{\left|\tilde{R}_X^2(f) - \tilde{R}_Y^2(f)\right|}{\min^2\left\{\tilde{R}_X(f), \tilde{R}_Y(f)\right\}}}, \tag{5}$$

in which n is the number of discrete frequency samples in the interval $\left[f_A\left(f_l\right), f_B\left(f_l\right)\right]$ and the commutative property $\gamma_{XY}\left(f_l\right) = \gamma_{YX}\left(f_l\right)$ applies. The $\gamma_{XY}\left(f_l\right)$ can be computed for an arbitrary pair of perpendicular cardinal or intercardinal directions (e.g., {N–S, E–W} or {NE–SW, SE–NW}), where the maximal value is denoted as $\gamma_{\max}\left(f_l\right)$. According to Matsushima et al. (2017), the directionality is noticeable when γ exceeds 0.7, and it is significant if γ exceeds 1.0.

Next, the directional dependency factor γ determines the magnitude but not the azimuth of the predominant directionality of the H/V peak. To describe the functional dependence of the H/V peak on azimuth, we express H/V spectral ratios $\tilde{R}_X(f)$ and $\tilde{R}_Y(f)$ in the functional notation $\tilde{R}(f,\varphi)$, in which angle φ is the azimuth of the respective horizontal direction. Note, this is just a change in notation that is favorable for the next operations. The functional dependence on an arbitrary azimuth φ is expressed using the arithmetic mean in the interval $\left[f_A\left(f_l\right), f_B\left(f_l\right)\right]$ as

$$\overline{R}\left(f_l,\varphi\right) = \frac{1}{n}\sum_{f=f_A(f_l)}^{f_B(f_l)} \tilde{R}(f,\varphi), \tag{6}$$

in which $\overline{R}\left(f_l,\varphi\right)$ is the directionally dependent mean H/V ratio of the peak at the frequency f_l. Because we use a finite number of horizontal directions, $\overline{R}\left(f_l,\varphi\right)$ is usually a sparsely sampled function in the φ domain. Hence, it is interpolated by the 1D cubic Spline interpolation into a dense grid, and the position of the maximal value is the desired azimuth of the predominant directionality of the H/V spectral peak $\vartheta\left(f_l\right)$

$$\vartheta\left(f_l\right) = \underset{\varphi}{\operatorname{argmax}}\left(\overline{R}\left(f_l,\varphi\right)\right). \tag{7}$$

3.3. S/B Earthquake Spectral Ratios

Next, let us assume one observation point on the ground surface (depth = 0) and the second reference point at a depth ζ (i.e., the borehole seismic array). Similarly to the location on the ground surface, the ground acceleration at the reference point can be described by three time series in orthogonal directions and respective complex spectral functions $X(f,\zeta)$, $Y(f,\zeta)$, and $Z(f,\zeta)$. Then, the S/B spectral ratio is

$$S_X(f,\zeta) = \frac{|X(f,0)|}{|X(f,\zeta)|}, \tag{8}$$

in which $S_X(f,\zeta)$ is the amplitude spectrum of the S/B transfer function. The formula for the S/B spectral ratio in the perpendicular horizontal direction, that is, $S_Y(f,\zeta)$, is expressed by substituting $Y(f,0)$ and $Y(f,\zeta)$ for $X(f,0)$ and $X(f,\zeta)$, respectively.

Similarly to H/V spectral ratios, S/B ratios should be statistically evaluated from several earthquakes and expressed by expected values. Then, the multi-event S/B spectral ratios $\tilde{S}_X(f,\zeta)$ and $\tilde{S}_Y(f,\zeta)$ are defined as median values from all events.

3.4. Ground Motion Characteristics

The strong ground motion can be quantitatively characterized by values of the Peak Ground Acceleration (PGA) and Peak Ground Velocity (PGV). The PGA is indicative of the peak forces at a material point, while PGV is related to the peak kinetic energy. Moreover, the PGV/ V_S has been proposed as a proxy (not in itself a directly related parameter) of the strain at a material point of a continuum body (Hill et al., 1993). Nevertheless, all of these parameters lack any information about the shaking duration and then also the total energy transferred by seismic waves. Hence, we use the Arias Intensity trace ($I_A(t)$; Arias, 1970) defined as

$$I_A(t) = \frac{\pi}{2g}\int_0^t u^2(\tau)\,\mathrm{d}\tau, \tag{9}$$

in which $u(t)$ is the one-component acceleration earthquake record, π is Archimedes' constant, g is the acceleration due to Earth's gravity, and τ is the time integration variable. The Arias Intensity trace is a time series determined from the full bandwidth of the earthquake spectrum, and it reaches its maximum at the total waveform duration T, that is, $I_A(T) = \max(I_A(t))$ where $t \in [0,T]$. Note, that the rate of change of Arias Intensity is proportional to $u^2(t)$, which is indicative of the squared force at a material point. In this paper, the total Arias Intensity $I_A(T)$ is a quantitative measure of the strong ground motion, the normalized Arias Intensity trace $I_A(t)/I_A(T)$ is used for the determination of the S-wave coda time window (i.e., 85%–100%) and the strong motion duration (i.e., 5%–95%), and the non-normalized Arias Intensity trace $I_A(t)$ is mathematically related to the time-dependent elastic softening during the 2024 M_J 7.6 Noto earthquake.

3.5. Signal Processing Procedure

The earthquake H/V spectral ratios were systematically evaluated at all selected sites located on the ground surface. First, records of regional earthquakes (epicentral distance of 0–200 km; see Figures S1 and S2 in Supporting Information S1) were rotated into Transverse, Radial, E–W, N–S, SE–NW, and NE–SW horizontal components, and their Arias Intensity traces were assessed by Equation 9. These were used for identification of the noise and S-wave coda time windows (before the first wave arrival and 85%–100% of the $I_A(T)$, respectively). All components (six horizontal and one vertical) and separate full, noise, and coda traces were processed by Fourier transformation (see Figure S5 in Supporting Information S1) and used for the computation of H/V spectral ratios by Equation 1. H/V ratios from all earthquakes were evaluated by Equation 2 to obtain statistically representative H/V spectral ratios. Then, we manually picked significant H/V peaks on multi-event median curves within the frequency range of 0.1–25 Hz (maximally four peaks per site) and assigned them an index (i.e., f_0, f_1, f_2, f_3). The f_0 is the main H/V peak of the lowest frequency in the considered frequency range at each site. Finally, we computed the directional dependency factor γ by Equation 5 and the predominant directionality azimuth ϑ by Equation 7 for all H/V peaks at all sites. This procedure was done separately for earthquakes before and 0–3 days after the 2024 M_J 7.6 Noto Peninsula earthquake (denoted as EQ24).

4. Results

The temporal evolution of the H/V spectral ratio is shown in Figure 2. In particular, it is the ISK015 site located in Anamizu Town (Ishikawa Prefecture) that experienced very strong ground shaking during the 2024 M_J 7.6 Noto earthquake (PGV >1 m/s). The earthquake H/V spectral ratio exhibited a temporally stable pattern during

21699356, 2025, 4, Downloaded from https://agupubs.onlinelibrary.wiley.com/doi/10.1029/2024JB029961 by Cochrane Japan, Wiley Online Library on [03/06/2025]. See the Terms and Conditions (https://onlinelibrary.wiley.com/terms-and-conditions) on Wiley Online Library for rules of use; OA articles are governed by the applicable Creative Commons License

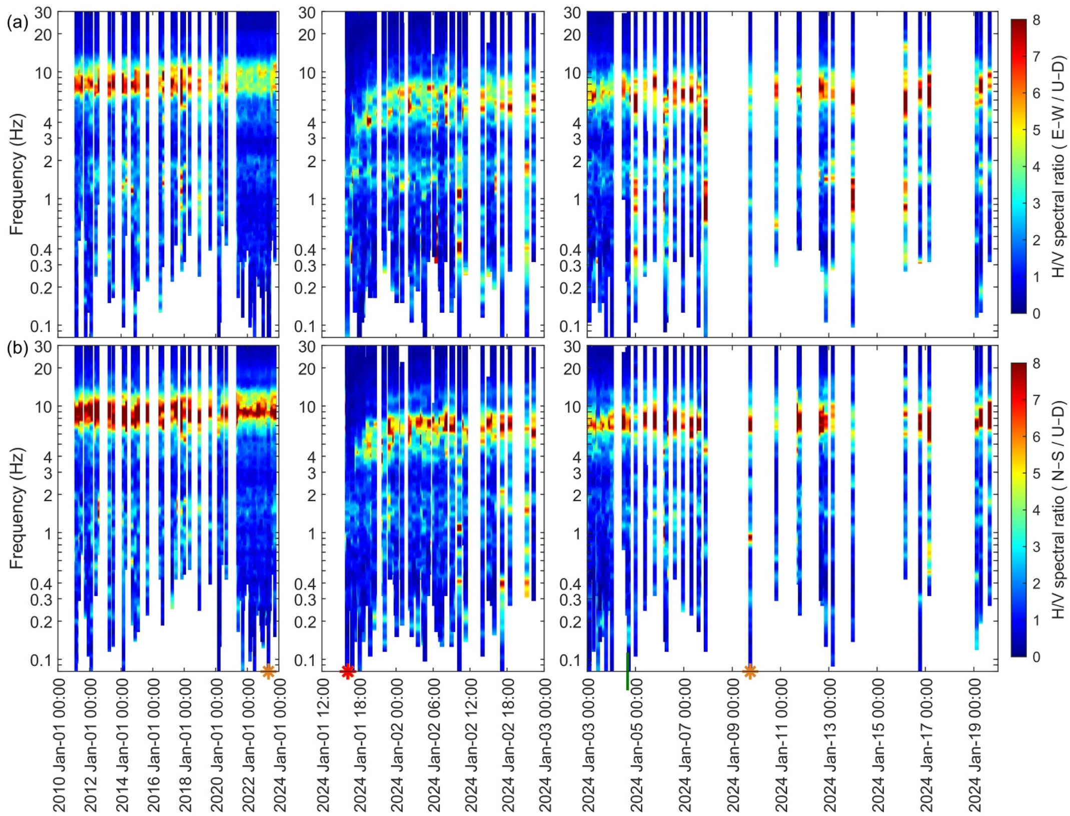

Figure 2. Example of the temporal evolution of H/V spectral ratio at the ISK015 site (Anamizu Town). The H/V spectral ratio is evaluated for full records of individual earthquakes by Equation 1 from (a) E–W and (b) N–S horizontal components. The left panels show the period before the 2024 M_J 7.6 Noto earthquake (2010–2024), the center panels show the period of 0–32 hr after the mainshock, and the right panels show 32–440 hr after the mainshock. The H/V spectral ratio for a single earthquake is shown by one colored column. The color has the meaning of a non-normalized H/V value (see colorbar). On the time axis in Japan Standard Time, the 2024 M_J 7.6 mainshock at 16:10 is marked by the red asterisk, orange asterisks are significant regional events with $M_J > 6$, and the green mark shows the time of 72 hr (3 days) after the mainshock.

14 years before the mainshock. With the occurrence of the M_J 7.6 mainshock, the pattern suddenly changed and stabilized in minutes-to-hours after the mainshock. Nevertheless, the H/V ratio pattern in the semi-stable phase after the mainshock was not the same as before (note the peak frequency drop from 8.85 to 6.97 Hz); hence, the site is expected to slowly recover to the initial state for the duration of months-to-years. Still, we can evaluate the multi-event H/V spectral ratios by Equation 2 for the stable period before and the semi-stable period 0–3 days after the 2024 M_J 7.6 Noto earthquake. An additional example is in Figure S6 in Supporting Information S1.

Regarding the multi-event H/V spectral ratios, the example in Figure 3a shows results for the ISK006 station (Shika municipality in Ishikawa Prefecture). This site has the main H/V peak at a frequency of 6.0 Hz. During the 2024 M_J 7.6 Noto earthquake, the station recorded maximal horizontal PGA of 26.8 m/s^2 (the largest measured PGA value for this earthquake), horizontal PGV of 0.83 m/s, and the frequency of the largest Fourier acceleration amplitude peak at 4.7 Hz (close yet smaller than the frequency of the H/V peak; see Figure S7 in Supporting Information S1). This site can be compared with the JMA914 station in Figure 3b, which is located about 3.65 km to the ESE direction. The JMA914 site has a lower frequency of the main H/V peak of about 2.6 Hz. During the M_J 7.6 earthquake, the station recorded a maximal horizontal PGA of 5.7 m/s^2 and a maximal horizontal PGV of 0.66 m/s. Contrasts between these two sites indicate that site effects play an important role during the strong ground shaking even for such nearby locations. Next, Figure 3c shows the H/V ratio at the JMAE10 station (Wajima City), and in Figure 3d, we show the TYMP19 station (Toyama City) with a very low frequency of the main H/V peak with a strong directionality (peak at 0.13 Hz).

21699356, 2025, 4, Downloaded from https://agupubs.onlinelibrary.wiley.com/doi/10.1029/2024JB029961 by Cochrane Japan, Wiley Online Library on [03/06/2025]. See the Terms and Conditions (https://onlinelibrary.wiley.com/terms-and-conditions) on Wiley Online Library for rules of use; OA articles are governed by the applicable Creative Commons License

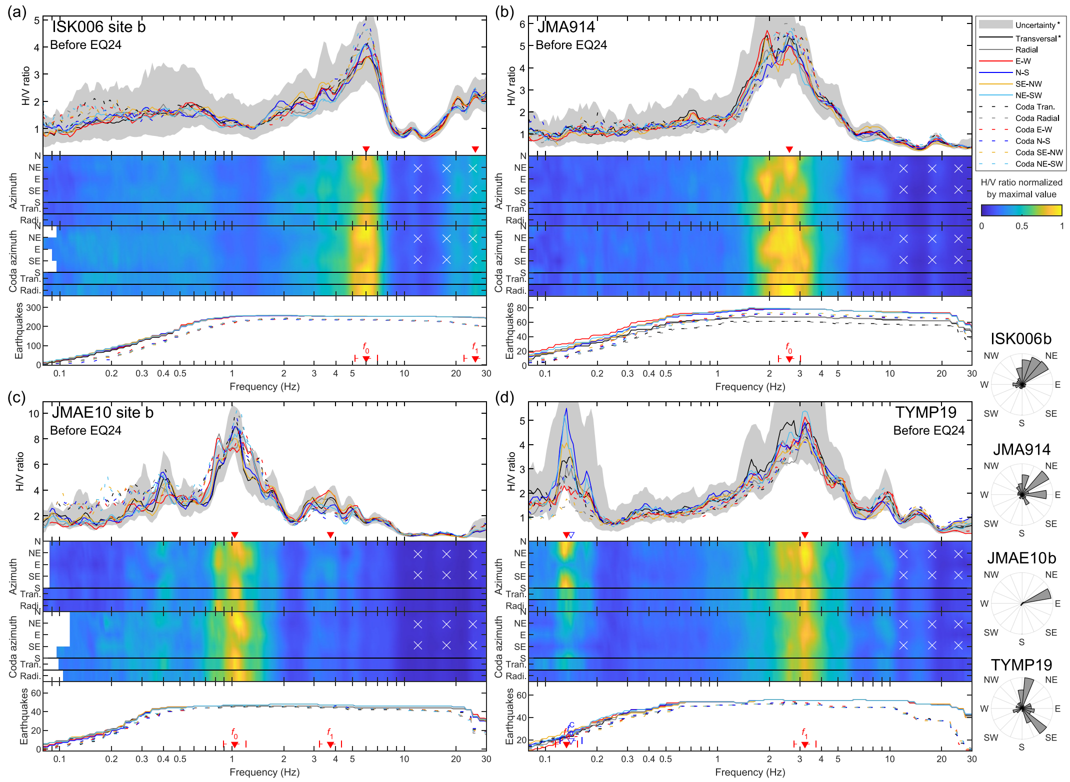

Figure 3. Examples of site-specific directionally dependent H/V spectral ratios at (a) ISK006, (b) JMA914, (c) JMAE10, and (d) TYMP19 sites before the 2024 M_J 7.6 Noto earthquake. The upper panel shows H/V curves for individual horizontal components (see legend), contour plots in the middle panels show directionally dependent H/V ratios normalized by maximal value (for both full and *S*-wave coda time windows), and the bottom panel shows number of contributing earthquakes per frequency. All sites have evaluated histograms of back azimuths to earthquake epicenters (right inset). H/V peaks f_l are shown by red triangles with bandwidth $[f_A(f_l), f_B(f_l)]$ highlighted by red errorbars. The white crosses in contour plots are to remind us that the high frequencies >10 Hz may but may not be influenced by sensor housing effects.

4.1. H/V Spectral Peaks

All H/V spectral peaks have assigned the frequency f_l, maximal H/V value, maximal directional dependency factor $\gamma_{\max}(f_l)$, and the directionality azimuth $\vartheta(f_l)$. We do not observe significant seasonal changes in these parameters because we use incident body waves from regional earthquakes in our analysis (not microtremor nor ambient noise sources). At the same time, we use up to 28 years of earthquake records having significant ground motion levels yet mostly within the elastic range, which provides us with sufficient statistical certainty. Then, we can assume that the determined site-specific parameters exhibit long-term stability before the 2024 M_J 7.6 Noto earthquake.

The spatial distribution of attributes of H/V spectral peaks is shown in Figure 4. Because we picked more than one significant H/V peak per site, we show separately low-frequency H/V peaks with $f_l < 0.8$ Hz (left panels) and high-frequency H/V peaks with $f_l \geq 0.8$ Hz (right panels). Peaks are probably related to fundamental resonance modes of several stratified layers, not higher resonance modes of one sedimentary layer. The low-frequency H/V peaks are likely related to a deep lithological interface of the seismological bedrock, while high-frequency ones originate from shallow near-surface layers. In Figure 4a, note sites with very low-frequency H/V peaks of 0.1–0.2 Hz located in the Kanazawa City (e.g., stations JMAE15, MTSM05, MTSM08), and along the Toyama Bay (e.g., stations TYM005, TYMH03, TYMP06, TYMP08, TYMP19, JMAE17, JMA533, TYMO). Indeed, these sites are situated on hundreds to thousands of meters thick geological formations of sediments and sedimentary rocks. In Figure 4b, the high-frequency H/V peaks of mainly 1–10 Hz are distributed across the whole study area, which reflects the variability of near-surface layers. Frequencies of our H/V peaks are consistent with the results of microtremor surveys in the Kaga, Ochigata, and Toyama Plains by Asano et al. (2015, 2020). Next, the

21699356, 2025, 4, Downloaded from https://agupubs.onlinelibrary.wiley.com/doi/10.1029/2024JB029961 by Cochrane Japan, Wiley Online Library on [03/06/2025]. See the Terms and Conditions (https://onlinelibrary.wiley.com/terms-and-conditions) on Wiley Online Library for rules of use; OA articles are governed by the applicable Creative Commons License

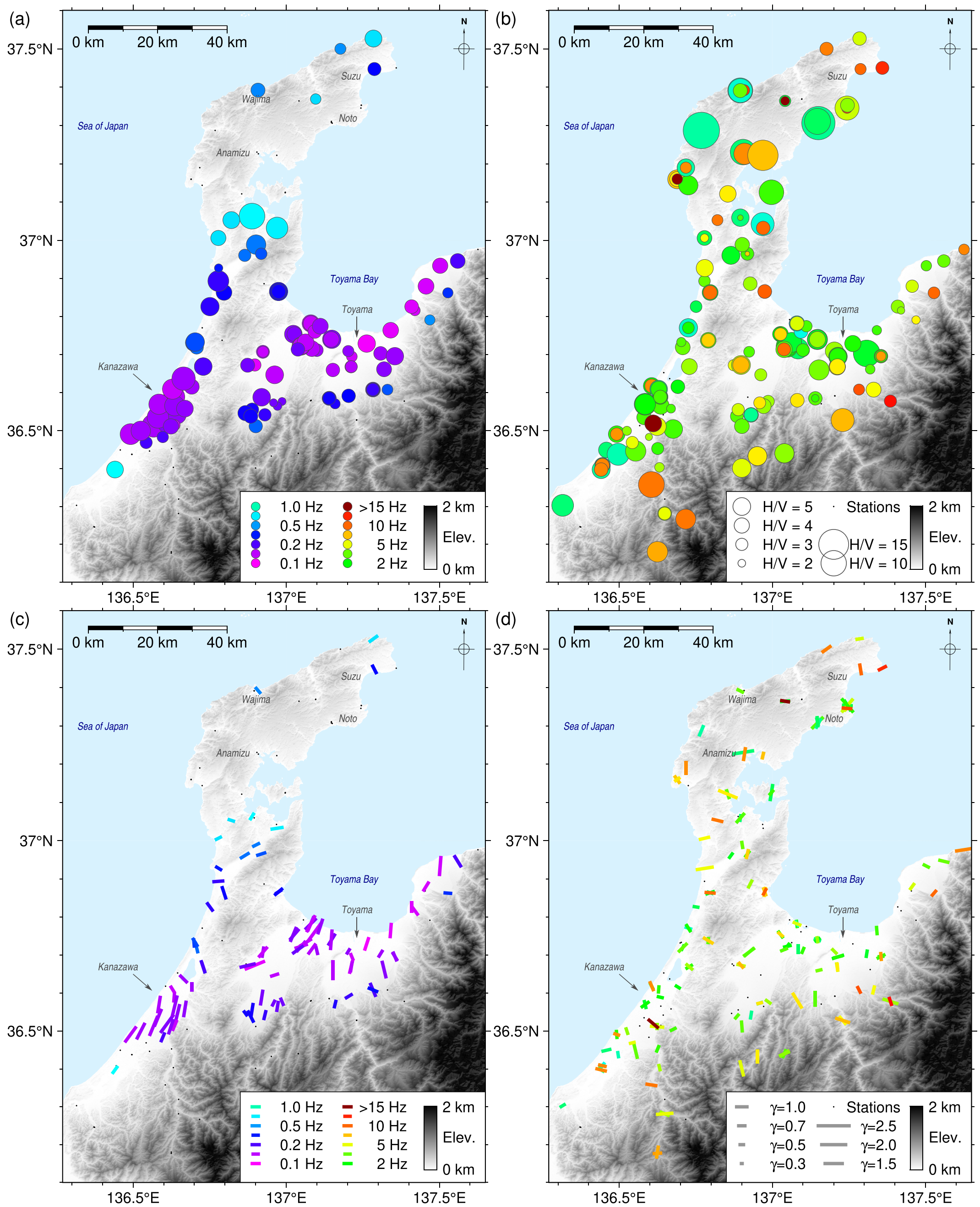

Figure 4. Spatial distribution of the frequency and directionality of observed H/V spectral peaks before the 2024 M_J 7.6 Noto earthquake. (a), (c) Low-frequency H/V peaks with $f_l < 0.8$ Hz, (b), (d) high-frequency H/V peaks with $f_l \geq 0.8$ Hz. The frequency is shown by color. In the upper row, the circle size has the meaning of the H/V value at the respective frequency. In the bottom row, the line segment size shows the value of the maximal directional dependency factor $\gamma_{\max}(f_l)$, and the line segment direction is the directionality azimuth $\vartheta(f_l)$. Line segments are centered in the station locations. Sites without H/V peaks in the respective frequency range are shown by black dots.

directionality of observed H/V spectral peaks show predominant directions that are parallel to basin edges. This feature is especially evident for low-frequency H/V peaks in Figure 4c. It may be the two-dimensional resonance effect of the basin infill caused by incident *SH*-waves (e.g., Bard & Bouchon, 1985; Roten et al., 2006). In particular, note the spatial distribution of the directionality in Kanazawa City, which creates a clear spatial pattern.

21699356, 2025, 4, Downloaded from https://agupubs.onlinelibrary.wiley.com/doi/10.1029/2024JB029961 by Cochrane Japan, Wiley Online Library on [03/06/2025]. See the Terms and Conditions (https://onlinelibrary.wiley.com/terms-and-conditions) on Wiley Online Library for rules of use; OA articles are governed by the applicable Creative Commons License

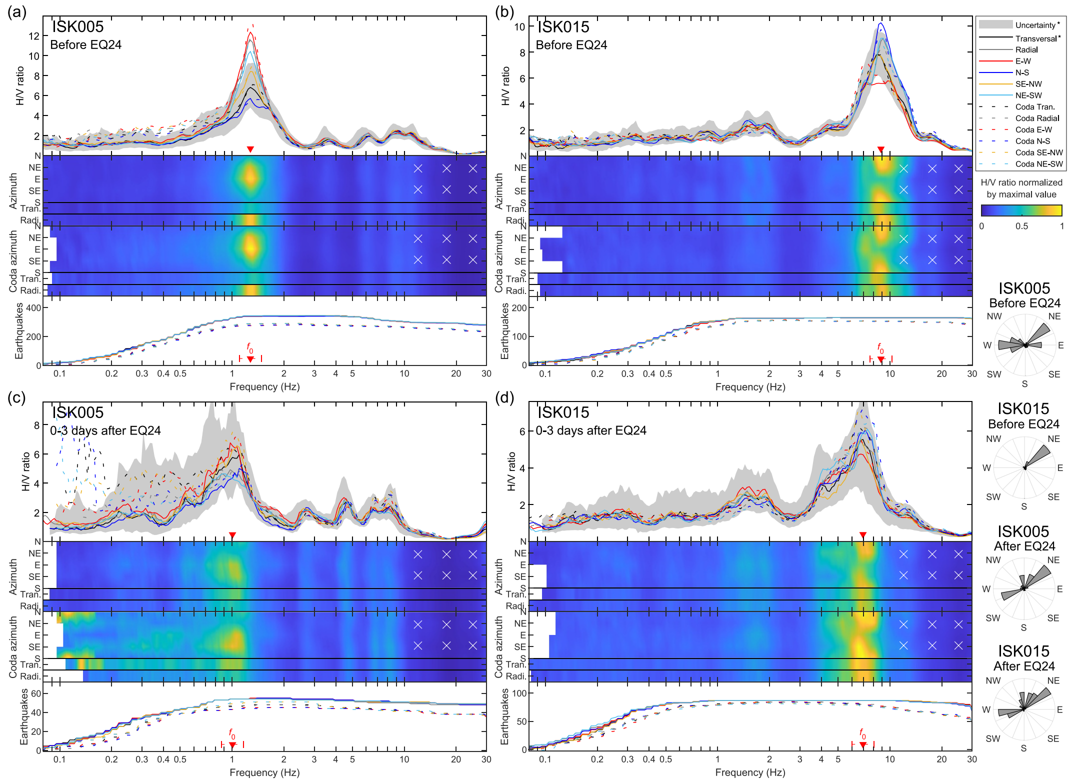

Figure 5. The long-lasting change—Examples of directionally dependent H/V spectral ratios at (a), (c) ISK005 and (b), (d) ISK015 sites before and after the 2024 M_J 7.6 Noto earthquake. In the upper row, the H/V spectral ratios are determined from regional earthquakes before the 2024 mainshock. In the bottom row, the H/V ratios are determined from aftershocks recorded during 0–3 days. Individual panel layout and meaning are the same as in Figure 3.

4.2. Long-Lasting Change After the M7.6 Earthquake

In Figures 3 and 4, we show results representing the linear site response before the 2024 M_J 7.6 Noto earthquake. Nevertheless, strong ground shaking can cause structural changes in near-surface layers, which can change the site response in the long term. The long-lasting change is mainly characterized by a change in the site-specific resonance frequency (e.g., Sawazaki et al., 2006). To investigate the possibility of the long-lasting change after the 2024 M_J 7.6 Noto earthquake, we evaluated multi-event H/V spectral ratios from aftershocks recorded 0–3 days after. Then, the quantitative comparison of H/V peaks from data before and after the mainshock expresses the long-lasting change in H/V peaks at individual sites. Note, that the long-lasting change may have a duration of several years (e.g., Okubo et al., 2024), but it should be the most prominent within a few days after the mainshock. Quantitatively, the relative change in H/V peak frequency (i.e., δf_l) is calculated by

$$\delta f_l = \left(\frac{f_l^{\text{after}}}{f_l^{\text{before}}} - 1 \right) \times 100[\%]. \tag{10}$$

Examples of H/V spectral ratios determined from earthquake waveforms recorded before and after the EQ24 mainshock are shown in Figure 5, and the spatial distribution of the long-lasting change in the site response is shown in Figure 6. In Figure 5, we show results for the ISK005 and ISK015 stations, which are located about 640 m from each other in a densely populated area of Anamizu Town. These two sites exhibit the most prominent after-before difference in H/V peak frequencies from all investigated sites. At the ISK005 site, the f_0 changed from 1.28 to 1.01 Hz, and at the second site it dropped from 8.85 to 6.97 Hz, that is, the relative change δf_l of -21% for both sites. Besides the frequency drop of the main peak, note the change in the overall shape of H/V ratios and the shift of minor peaks above the f_0 toward low frequencies (all shallower structures with the higher resonance frequency are affected). Still, all the horizontal directions change jointly and the site-specific

21699356, 2025, 4, Downloaded from https://agupubs.onlinelibrary.wiley.com/doi/10.1029/2024JB029961 by Cochrane Japan, Wiley Online Library on [03/06/2025]. See the Terms and Conditions (https://onlinelibrary.wiley.com/terms-and-conditions) on Wiley Online Library for rules of use; OA articles are governed by the applicable Creative Commons License

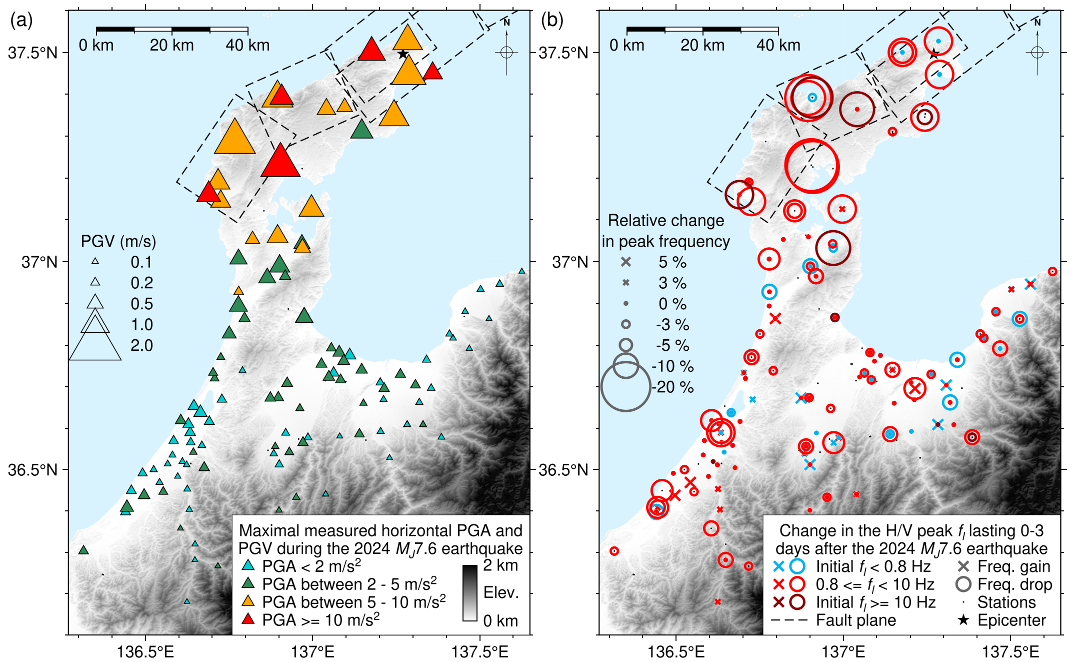

Figure 6. Maximal measured Peak Ground Acceleration (PGA) and Peak Ground Velocity (PGV), and the long-lasting change in site response. (a) Shows the spatial distribution of the maximal PGA and PGV values measured at horizontal components during the 2024 M_J 7.6 Noto earthquake. The PGV is shown by triangle size and the PGA by filling color. Sites without the mainshock data are shown by black dots. (b) Shows the spatial distribution of the change in the H/V peak frequency lasting 0–3 days after the M_J 7.6 mainshock. The frequency gains or drops are shown by cross or circle marks, respectively. The mark size is proportional to the magnitude of δf_l, and the mark color shows the frequency (see legend). The assumed M_J 7.6 mainshock fault planes are adapted from Asano and Iwata (2024).

predominant directionality is preserved after the strong shaking. During the 2024 M_J 7.6 Noto earthquake, the ISK005 station recorded a maximal horizontal PGA of 11.5 m/s^2 and PGV of 1.47 m/s. The ISK015 station recorded a maximal horizontal PGA of 9.8 m/s^2 and PGV of 1.02 m/s. Note, that the most prominent long-lasting change in the site response is correlated with high-PGV sites.

Next, in Figures S8 and S9 in Supporting Information S1 are the results for surface sensors of ISKH02 and ISKH03 stations. These two stations are located in the northern part of the Noto Peninsula (Noto municipality) which was uplifted about 1 m during the 2024 earthquake. At the ISKH02 site, the f_0 at 1.67 Hz is unchanged before and after the mainshock, while the f_1 changed from 19.19 to 16.54 Hz (i.e., the relative change δf_l of -14%). This means that the long-lasting change in site response is limited to a very shallow layer with a depth of a few meters (related to f_1) and not related to the crustal uplift, while the underlying lithological layer (related to f_0) is unchanged at this site. At the ISKH03 site, we found an interesting feature of the splitting of the f_0 peak into two peaks after the 2024 earthquake. The frequencies of these new peaks are distributed around the original one (4.46 Hz peak changed to 3.96 and 4.73 Hz peaks), and it may be caused by a stratification or a lateral inhomogeneity of the change in predominant frequency. Additional examples are in Figures S10–S14 in Supporting Information S1.

The spatial distribution of the long-lasting site-response change is shown in Figure 6b through the relative change in H/V peak frequency δf_l by Equation 10. Because δf_l values were evaluated from various H/V peaks, we divided them into three groups based on the initial peak frequency that is distinguished by color (groups with $f_l < 0.8$ Hz, $0.8 \leq f_l < 10$ Hz, and $f_l \geq 10$ Hz). Then, we can distinguish effects in deep, shallow, and very-shallow layers. The spatial distribution of δf_l in Figure 6b implies that the deep lithological layers are not significantly affected by the strong ground shaking while shallow layers are (compare sizes of blue and red marks). At higher frequencies >0.8 Hz, the H/V peaks exhibit long-lasting drops of their frequencies that are correlated with PGV values observed during the strong shaking (compare circle sizes with sizes of triangles in Figure 6a). Note, that sites with the largest frequency drops experienced the largest PGV values during the M_J 7.6 mainshock (i.e., sites in the

21699356, 2025, 4, Downloaded from https://agupubs.onlinelibrary.wiley.com/doi/10.1029/2024JB029961 by Cochrane Japan, Wiley Online Library on [03/06/2025]. See the Terms and Conditions (https://onlinelibrary.wiley.com/terms-and-conditions) on Wiley Online Library for rules of use; OA articles are governed by the applicable Creative Commons License

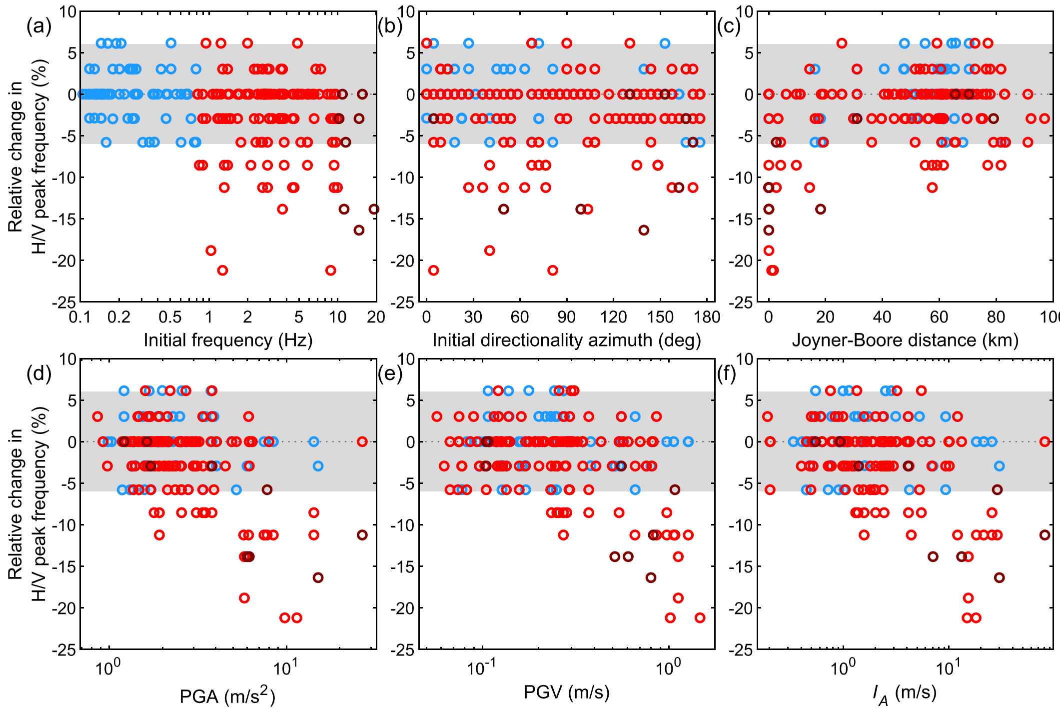

Figure 7. The dependency of the long-lasting change in site response on selected ground motion characteristics. The relative long-lasting predominant frequency change δf_l is shown as dependent on (a) initial frequency of the H/V peak, (b) initial azimuth of predominant H/V peak directionality, (c) Joyner-Boore distance from the M_J 7.6 mainshock fault plain, (d) maximal horizontal PGA, (e) PGV, and (f) total Arias Intensity $I_A(T)$ measured during the M_J 7.6 mainshock. The mark color shows the predominant frequency (blue: $f_i < 0.8$ Hz, red: $0.8 \le f_i < 10$ Hz, dark-red: $f_i \ge 10$ Hz). The gray area is an insignificant δf_l change that is within the estimated uncertainty ±6%.

Anamizu Town). This indicates that the long-lasting drop in the H/V peak frequency is a phenomenon related to the strong ground shaking. Further, in the southern part of the study area, the long-lasting change in the H/V peak frequency is mild or none. The mild long-lasting frequency gains and drops have no pattern and are within the estimated uncertainty of H/V picks ±6% (see Table S1 in Supporting Information S1). Exceptions are isolated sites with significant frequency drops that may be related to the liquefaction phenomenon. For instance, the JMAE15 site in the Kanazawa City ($\delta f_l = -11\%$) and the JMA536 site in the Komatsu City ($\delta f_l = -9\%$) are both located in zones with the highest liquefaction risk level estimated from the regional liquefaction susceptibility map (Ministry of Land et al., 2013). According to the liquefaction susceptibility map, these two zones of high liquefaction risk are the most prominent from both Ishikawa and Toyama prefectures. This means that seismic monitoring stations in these zones are more likely affected by the liquefaction phenomenon, as also supported by observed macroscopic signs.

Next, we evaluated the dependency of the long-lasting predominant frequency change δf_l on selected ground motion characteristics. First, in Figure 7a, we show the dependency of δf_l on the initial frequency of H/V peaks (i.e., the frequency before the M_J 7.6 mainshock). This supports that the low-frequency peaks (blue color; deep lithological layers) are not significantly affected by the strong ground shaking while high-frequency peaks are (red color; shallow layers). The dependency on the initial azimuth of H/V peak directionality in Figure 7b shows no pattern, which implies an omnidirectional site effect (i.e., an effect different from the directionality of the earthquake wave field). In Figure 7c, there is a strong dependency on the Joyner-Boore distance (Joyner & Boore, 1981) from the M_J 7.6 mainshock (the fault plain model is adapted from Asano & Iwata, 2024). The most significant long-lasting changes are located at sites in the Joyner-Boore distance <20 km. Further, Figures 7d–7f show relations with the PGA, PGV, and total Arias Intensity measured during the M_J 7.6 mainshock, respectively. Indeed, the larger long-lasting changes are correlated with higher ground motion levels. In particular, note the clear dependency on the maximal horizontal PGV, which implies that a minimal PGV value to be able to cause a detectable long-lasting change is approximately 0.2 m/s, and a significant site-response change can be produced if

21699356, 2025, 4, Downloaded from https://agupubs.onlinelibrary.wiley.com/doi/10.1029/2024JB029961 by Cochrane Japan, Wiley Online Library on [03/06/2025]. See the Terms and Conditions (https://onlinelibrary.wiley.com/terms-and-conditions) on Wiley Online Library for rules of use; OA articles are governed by the applicable Creative Commons License

21699356, 2025, 4, Downloaded from https://agupubs.onlinelibrary.wiley.com/doi/10.1029/2024JB029961 by Cochrane Japan, Wiley Online Library on [03/06/2025]. See the Terms and Conditions (https://onlinelibrary.wiley.com/terms-and-conditions) on Wiley Online Library for rules of use; OA articles are governed by the applicable Creative Commons License

PGV >0.5 m/s. The estimated minimal PGA value to be able to cause a detectable long-lasting site-response change is approximately 2.0 m/s^2 (200 gal). Still, the site-response change may or may not occur based on site-specific conditions (i.e., the dependence on V_{S30} as shown by Esfahani et al., 2024).

4.3. Short-Lasting Change During the M7.6 Earthquake

In the previous section, we investigated the long-term change in H/V spectral peaks lasting 0–3 days after the 2024 M_J 7.6 Noto earthquake, while we ignored the site-specific nonlinear behavior during the mainshock itself. In this section, we focus on the short-lasting coseismic change during the nonlinear strong ground shaking with a duration of tens of seconds. Similar to the long-lasting change, the short-lasting one is characterized by a drop in the site-specific resonance frequency (Iwata et al., 2008; Wu & Peng, 2011), which may be related to a drop in the shear modulus (Pavlenko & Irikura, 2006). It means that the shape of the stress–strain hysteresis loop changes with time during the strong shaking; hence, properties of the ground motion nonlinearity are nonstationary.

To investigate the nonstationary behavior, we evaluated the short-lasting change in H/V spectral ratios from records of the 2024 M_J 7.6 Noto mainshock. First, we prepared short-period spectrograms for all components by the short-time Fourier transform (e.g., Gröchenig, 2001) using a 15-s-long Hann window; then, we computed the nonstationary H/V spectral ratios smoothed in the frequency domain by the Konno-Ohmachi window (Konno & Ohmachi, 1998). Examples of resultant nonstationary H/V spectral ratios are shown in Figure 8. The nonstationary H/V spectral ratios were calculated for all sites with available mainshock waveforms; nevertheless, only some sites exhibit a significant nonstationary behavior (i.e., a fast change in H/V ratios in time). The nonstationary behavior identified during the M_J 7.6 mainshock is.

- Clear and strong at sites ISK005, ISK015, ISKH03, JMAE10 b, ISKP35 b, and ISKP38.
- Unclear but probably significant at sites ISK001, ISK002, ISK003 b, ISKH01, JMA914, JMACCA, and ISKP41 b.
- Weak but evident at sites ISK006 b, ISK007, ISK008, ISK011, ISKH04, JMA535, JMA915 b, JMAE15, JMAE17, ISKP28, ISKP29, ISKP32, ISKP34, ISKP36, ISKP40 b, TYMP02 b, TYMP12, and MTSM05.

Note that sites with a strongly nonstationary behavior identified during the M_J 7.6 mainshock correlate with sites having large long-lasting frequency drops shown in Figure 6b (i.e., the northern part of the Noto Peninsula and potentially liquefied distant sites). The example in Figure 8a shows the nonstationary H/V spectral ratios at the ISK005 site (Anamizu Town). This free-field site has a near-surface profile consisting of clayey soil (depth of 0–1.2 m), peat (depth of 1.2–9.6 m), silt (depth of 9.6–11.8 m), sand (depth of 11.8–16.1 m), gravel (depth of 16.1–16.9 m), and rock (depth >16.9 m). The frequency of the H/V peak (the initial frequency of 1.28 Hz) decreased simultaneously with the strong shaking in all horizontal directions (see SE–NW and NE–SW components in Figure S15 in Supporting Information S1). Then, the frequency of the H/V peak was recovering as a logarithmic function several tens of seconds after the end of the strong shaking. This is a remarkable result that implies that the frequency drop is directly related to the strong ground shaking and it is an omnidirectional site-related phenomenon (i.e., related to the transversely isotropic change in material properties). Further, the frequency drop cannot be related to a postseismic fluid flow in near-surface layers because such an effect would be delayed in time after the strong shaking. Next, the ISK015 site (Figure 8b) exhibits a very strong drop in the H/V peak frequency with a very slow recovery rate (not recovered even 250 s after the strong shaking). It seems to be an exceptional site where the H/V peak with the initial frequency of 8.85 Hz temporarily disappeared completely. This site is situated in a small artificial depression (see Figure S36 in Supporting Information S1) with a near-surface profile consisting of sand (depth of 0–0.9 m), silt (depth of 0.9–1.7 m), rock (depth of 1.7–5.8 m), and hard rock (depth >5.8 m). Hence, it seems that the uppermost layers are locally liquefied. From the temporal evolution of the H/V spectral ratio at the ISK015 site in Figure 2, the H/V spectral ratio recovered to the semi-stable state with the predominant frequency of 6.97 Hz in approximately 5–8 hr after the strong shaking. Additional examples are in Figures S16–S22 in Supporting Information S1.

In addition, we evaluated the short-lasting coseismic change in H/V spectral ratios from records of the 2007 M_J 6.9 and 2023 M_J 6.5 earthquakes (see Figures S23–S26 in Supporting Information S1). Indeed, there is just a minor (2007 earthquake) or no (2023 earthquake) frequency change during these events, even at ISK005 and ISK015 sites. Hence, the short-lasting change in H/V spectral ratios is a site effect that can be attributed to the strong ground shaking.

Journal of Geophysical Research: Solid Earth 10.1029/2024JB029961

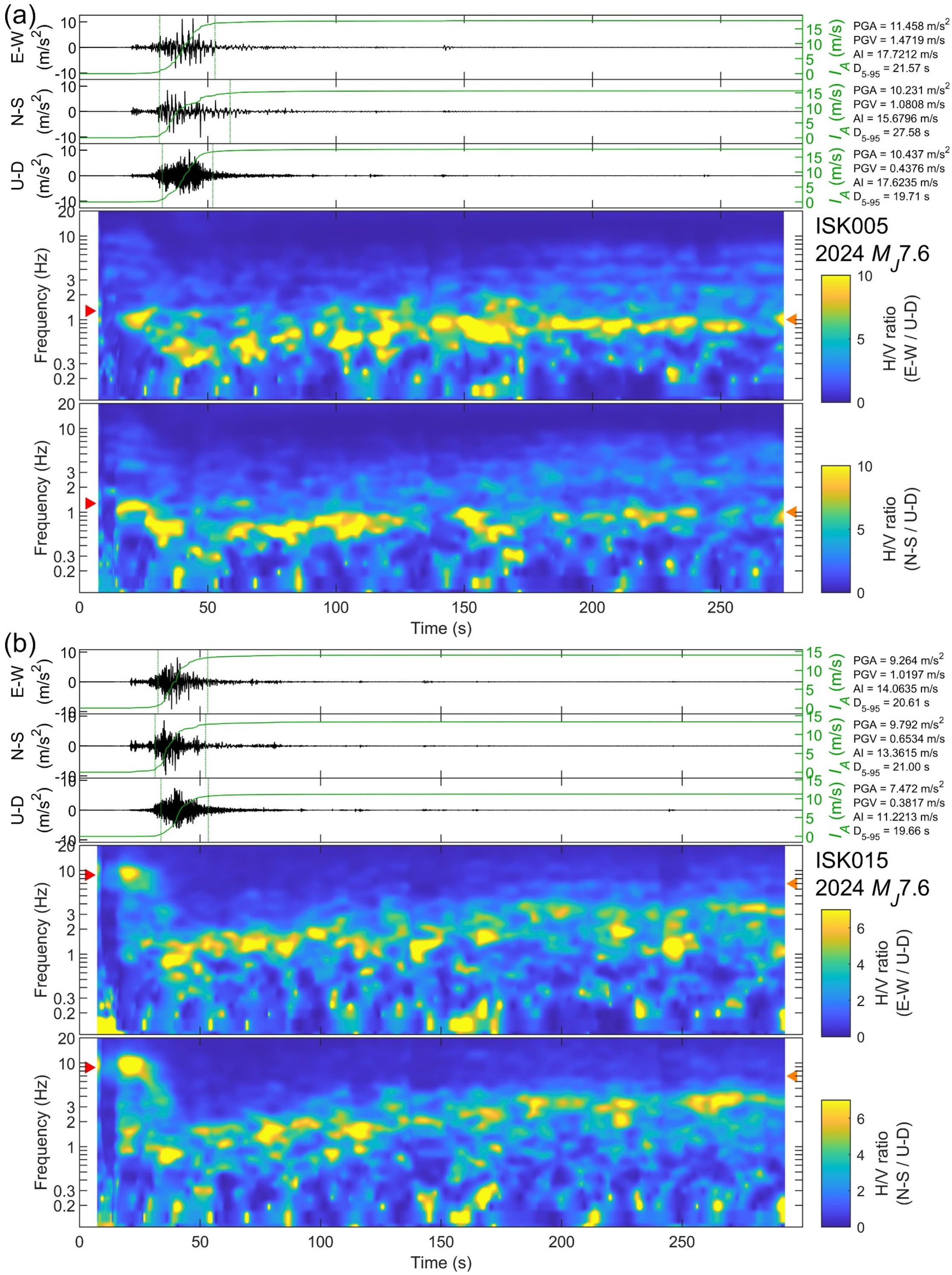

Figure 8. The short-lasting change—The nonstationary H/V spectral ratios during the 2024 M_J 7.6 Noto earthquake at (a) ISK005 and (b) ISK015 sites in Anamizu Town. The upper panels show measured acceleration waveforms in E–W, N–S, and Up–Down directions (black curves). The green curves are Arias Intensity traces $I_A(t)$ computed by Equation 9. The strong motion duration D_{5-95} is defined by 5%–95% of $I_A(T)$, which is highlighted by green dashed vertical lines. The middle and bottom panels show nonstationary H/V spectral ratios determined from E–W and N–S horizontal components, respectively. The value of H/V spectral ratios is shown by color scale. The red and orange triangles are frequencies of H/V peaks before and after the M_J 7.6 mainshock, respectively (i.e., the long-lasting change). Panels have a joint time axis.

21699356, 2025, 4, Downloaded from https://agupubs.onlinelibrary.wiley.com/doi/10.1029/2024JB029961 by Cochrane Japan, Wiley Online Library on [03/06/2025]. See the Terms and Conditions (https://onlinelibrary.wiley.com/terms-and-conditions) on Wiley Online Library for rules of use; OA articles are governed by the applicable Creative Commons License

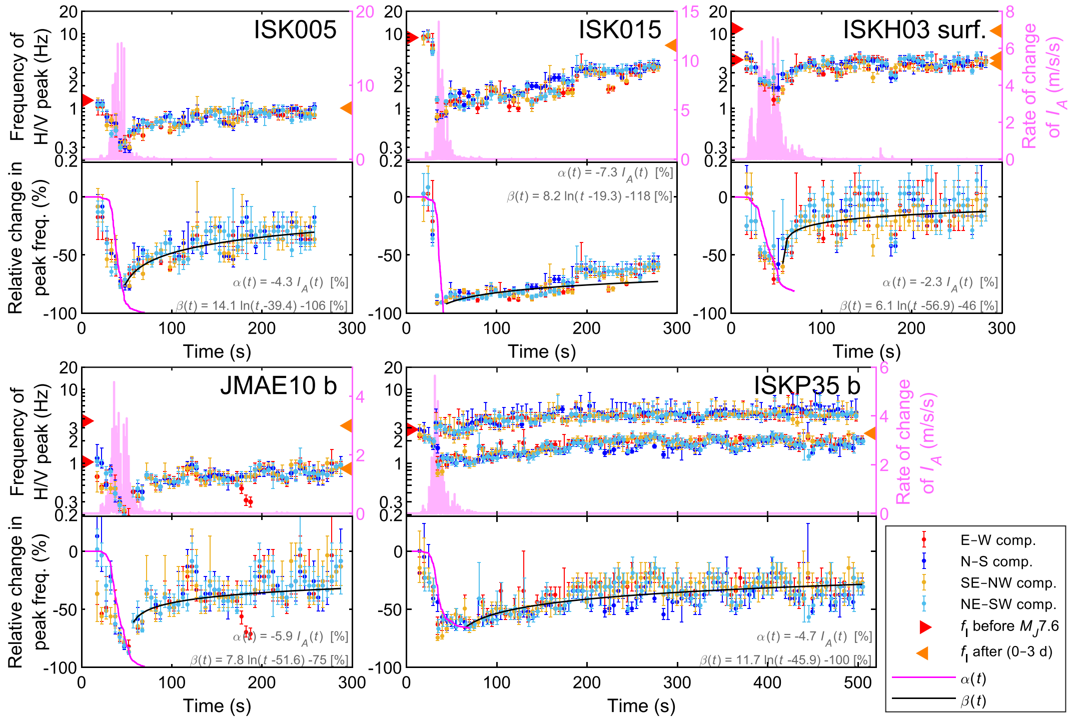

Figure 9. The short-lasting change—The temporal evolution of H/V spectral peaks during the 2024 M_J 7.6 Noto earthquake at five sites with a strongly nonstationary behavior. Each site has assigned a pair of panels with a joint time axis (station codes are displayed in upper panels). The upper panels show the observed time-dependent H/V peak frequency $f_l(t)$ and bottom panels show its relative change $\delta f_l(t)$ from Equation 11. The empirical data are shown by colored dots supplemented with errorbars. The color has the meaning of used horizontal component (see legend). In the upper panels, the pink curve is the rate of change of the non-normalized Arias Intensity trace in the total horizontal direction. In the bottom panels, magenta and black curves are theoretical functions $\alpha(t)$ and $\beta(t)$ with the best fit to empirical data.

To quantitatively evaluate the short-lasting change in the site response, we modified Equation 10 by using the dependency on time. The time-dependent relative change in H/V peak frequency $\delta f_l(t)$ is expressed by

$$\delta f_l(t) = \left(\frac{f_l(t)}{f_l(0)} - 1\right) \times 100[\%], \tag{11}$$

in which $f_l(t)$ is time-dependent H/V peak frequency and $f_l(0)$ is the initial value of peak frequency before the mainshock. Then, an extreme value of frequency drop δf_l^* is computed as

$$\delta f_l^* = \min_t \delta f_l(t). \tag{12}$$

We manually picked the time-dependent H/V peak frequency $f_l(t)$ including its uncertainty at all sites with clear nonstationary behavior. The picking was performed in all horizontal directions separately, and the resultant functions $f_l(t)$ and $\delta f_l(t)$ are displayed in Figure 9. Note, that all horizontal directions exhibit a similar pattern of the time-dependency (i.e., an omnidirectional effect). As may be expected, short-lasting extreme frequency drops δf_l^* are much stronger (values from -93% to -71%) than values of the long-lasting frequency change δf_l. Extreme frequency drops, long-lasting change, and maximal horizontal PGA and PGV values are summarized in Table 2. Except for the ISK015 site (i.e., discussed above), the extreme frequency drop values correlate with the PGV. At the ISKP35b site, we picked the temporal evolution of $f_0(t)$ and one additional H/V peak at a higher frequency (see Figure 9). The additional high-frequency peak follows the pattern of the $f_0(t)$ at this site; hence, the shallower structure is affected as well. At the ISKP38 site that recorded the largest PGV value for this earthquake, the short-lasting extreme frequency drop δf_l^* has value of -70% (see Figure S19 in Supporting Information S1).

21699356, 2025, 4, Downloaded from https://agupubs.onlinelibrary.wiley.com/doi/10.1029/2024JB029961 by Cochrane Japan, Wiley Online Library on [03/06/2025]. See the Terms and Conditions (https://onlinelibrary.wiley.com/terms-and-conditions) on Wiley Online Library for rules of use; OA articles are governed by the applicable Creative Commons License

21699356, 2025, 4, Downloaded from https://agupubs.onlinelibrary.wiley.com/doi/10.1029/2024JB029961 by Cochrane Japan, Wiley Online Library on [03/06/2025]. See the Terms and Conditions (https://onlinelibrary.wiley.com/terms-and-conditions) on Wiley Online Library for rules of use; OA articles are governed by the applicable Creative Commons License

Table 2
Observed and Parameterized Peak Frequency Change During the M_J 7.6 Earthquake

Site	PGA (m/s^2)	PGV (m/s)	δf_l (%)	δf_l^* (%)	m_α (s/m)	m_β (−)	m_t (s)	m_c (−)
ISK005	11.5	1.47	−21	−79	−4.3	14.1	−39.4	−106
JMAE10 b	5.8	1.13	−19	−79	−5.9	7.8	−51.6	−75
ISKH03 surf.	7.8	1.08	−11	−74	−2.3	6.1	−56.9	−46
ISK015	9.8	1.02	−21	−93	−7.3	8.2	−19.3	−118
ISKP35 b	6.1	0.86	−11	−71	−4.7	11.7	−45.9	−100

Note. Values of δf_l and δf_l^* are the observed long-lasting and short-lasting predominant frequency drops, respectively. Parameters m describe the theoretical model of the short-lasting peak frequency change.

Further, the time-dependent site-response change can be divided into the elastic softening and recovery phases. The breaking point is the time when the extreme frequency drop occurs. Because elastic softening is an unexplored phenomenon so far, we tackle this issue here. In the softening phase, the change in time-dependent peak frequency $f_l(t)$ seems to be related to the rate of change of Arias Intensity trace that is shown by the pink curve in Figure 9. As the rate of change of $I_A(t)$, we use the Euclidean norm from two non-normalized Arias Intensity traces for E–W and N–S horizontal components. Then, the rate of change of the Arias Intensity trace is proportional to the squared acceleration in a horizontal direction, which is proportional to the squared lateral force. This means that the elastic softening is probably governed by the lateral force applied to near-surface layers. To express the short-lasting softening and recovery quantitatively, we fit the empirical function $\delta f_l(t)$ by theoretical ones $\alpha(t)$ and $\beta(t)$ defined as

$$\alpha(t) = m_\alpha\, I_A(t), \tag{13}$$

$$\beta(t) = m_\beta \ln(t + m_t) + m_c, \tag{14}$$

in which m_α, m_β, m_t, and m_c are model parameters, and functional values represent the relative change in percentage (%). The theoretical functions $\alpha(t)$ and $\beta(t)$ are fitted to relative change data from the softening and recovery phases, respectively (for details on the inversion method see Text S2 and Figure S27 in Supporting Information S1). The resultant theoretical functions with the best least-square fit are shown by magenta and black lines in Figure 9, and the maximum likelihood model parameters are summarized in Table 2. Statistics from five sites with strongly nonstationary behavior show that the softening parameter m_α has median and mean values of −4.7 and −4.9 s/m, respectively (with a standard deviation of 1.9 s/m); and the recovery rate parameter m_β has median and mean values of 8.2 and 9.6, respectively (with a standard deviation of 3.2). These values quantitatively describe the observed short-lasting softening and recovery at near-surface soil layers, which may be used for prediction purposes (e.g., earthquake scenario modeling for engineering purposes).

4.4. Changes in S/B Spectral Ratios

Earthquake H/V spectral ratios are approximately related to the fundamental resonant frequencies of near-surface sedimentary layers; nevertheless, the relation may be complicated by the complex nature of the wavefield. Hence, we provide here a supporting analysis of Surface-to-Borehole (S/B) transfer functions at regional KiK-net stations.

Similarly to H/V ratios, the multi-event S/B spectral ratios $\tilde{S}_X(f,\zeta)$ and $\tilde{S}_Y(f,\zeta)$ were evaluated separately for earthquakes that occurred before, 0–3 days after, and 3–31 days after the 2024 M_J 7.6 Noto earthquake. An interpretation of S/B peaks is complicated by the interference of upward and downward body waves reflected by the ground surface; hence, these peaks are not equal to the H/V peaks. Nevertheless, we can evaluate long-lasting relative changes δf_l in S/B peak frequency by using Equation 10.

Resultant S/B spectral ratios and long-lasting relative changes in peak frequency are shown in Figure 10 for six borehole sites. Also, relative changes in S/B peak frequency (circle and diamond marks) are compared with the long-lasting relative change in H/V peak frequency (asterisk marks). The S/B spectral ratios exhibit small yet noticeable differences between the three used time spams, which is characterized by a reduction of peak frequency

21699356, 2025, 4, Downloaded from https://agupubs.onlinelibrary.wiley.com/doi/10.1029/2024JB029961 by Cochrane Japan, Wiley Online Library on [03/06/2025]. See the Terms and Conditions (https://onlinelibrary.wiley.com/terms-and-conditions) on Wiley Online Library for rules of use; OA articles are governed by the applicable Creative Commons License

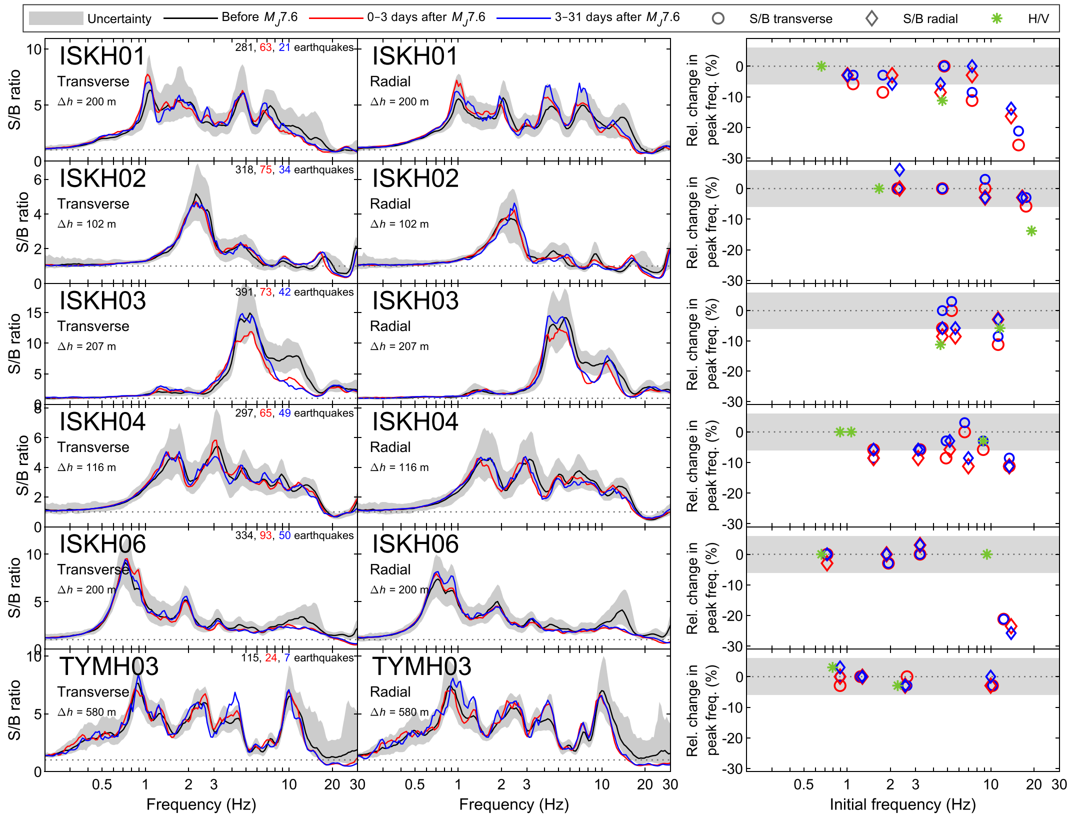

Figure 10. The long-lasting change in S/B earthquake spectral ratios at KiK-net sites. Station codes are displayed in individual panels together with the depth of sensors deployed in boreholes Δh. The S/B spectral ratios for Transverse and Radial horizontal components (left and center panels, respectively) were computed from earthquakes that occurred before (black), 0–3 days after (red), and 3–31 days after (blue) the 2024 M_J 7.6 Noto earthquake. Right panels show long-lasting relative changes in S/B peak frequency computed by Equation 10 for all peaks identified separately at Transverse and Radial components (circle and diamond marks, respectively). For comparison purposes, the long-lasting relative changes in H/V peak frequency are shown by green asterisk marks (determined in previous sections). The gray area is a zone of an insignificant frequency change of ±6%.

after the M_J 7.6 Noto earthquake (δf_l values in the range from −26% to 6%). The long-lasting drop in frequency is noticeable, especially at ISKH01, ISKH03, and ISKH04 sites (δf_l values around −10% at the frequency range of 0.8–10 Hz), in which the first two sites have also measured significant long-lasting frequency drops of H/V peaks. The relative change in the S/B frequency is larger for high-frequency peaks than low-frequency ones, which is also consistent with results for H/V peaks.

5. Physical Interpretation

The empirical data provided evidence that the 2024 M_J 7.6 Noto earthquake caused short- and long-lasting changes in the H/V peak frequency. Here, we provide a possible physical interpretation of this phenomenon supplemented by numerical modeling. First, let us formulate an idealistic hypothesis.

For simplicity, let us assume a single planar layer of sediments situated on a rigid rock (mathematical half-space). From the physical principle of standing waves (Faraday, 1831), the maximal resonance amplitudes of body waves are expected at odd multiples of a quarter wavelength (QWL; Ibs-von Seht & Wohlenberg, 1999; Joyner et al., 1981). Then, the resonance frequency f_S of body *SH*-waves on the sedimentary layer is

$$f_{S,i} = \frac{(2i+1)\,V_S}{4h}, \tag{15}$$

10.1029/2024JB029961

in which V_S is the S-wave velocity of the sedimentary layer, h is its thickness, and i is the resonance mode ($i \in \mathbb{N}$, but the most prominent is the fundamental resonance mode with $i = 0$). Note, that higher resonance modes with $i > 0$ are considered here just for mathematical completeness but are observed rarely. The observed higher resonance frequencies usually originate from a multilayer stratification. Also note, that for the validity of Equation 15, the presence of a free surface on the top of the profile is crucial. Then, if the resonance frequency of body waves $f_{S,i}$ suddenly changes while a negligible change in sedimentary layer thickness, we derive that

$$\frac{f_{S,i}^{\text{after}}}{f_{S,i}^{\text{before}}} = \frac{V_S^{\text{after}}}{V_S^{\text{before}}}, \tag{16}$$

in which parameters labeled as "before" and "after" refer to semi-stationary states before and after a sudden change caused by strong ground shaking. Note, that the ratio in Equation 16 is the same for all resonance modes. Next, we can assume that the frequency of earthquake H/V spectral peak f_l is almost the same as the SH-wave resonance frequency in this theoretical model ($f_l \approx f_{S,i}$), and then

$$\frac{V_S^{\text{after}}}{V_S^{\text{before}}} \approx \frac{f_l^{\text{after}}}{f_l^{\text{before}}} = \frac{\delta f_l}{100[\%]} + 1. \tag{17}$$

Note, that for the validity of Equation 17, only a proportionality between frequencies f_l and $f_{S,i}$ is sufficient ($f_l \propto f_{S,i}$). This means, that observed drops and subsequent recovery of H/V peak frequency can be physically explained by drops and recovery of near-surface S-wave velocity. Further, Equation 17 expresses the relation between the relative change in H/V peak frequency δf_l and change in S-wave velocity for a single sedimentary layer on a rigid rock, which is a rather idealistic model. In reality, an exact value of the S-wave velocity change will be influenced by the multilayer stratification of near-surface layers, changes in layer thicknesses by compaction, and a possible difference between frequencies of H/V peaks and SH-wave resonances.

Next, the value of S-wave velocity is related to the material properties of a medium by

$$V_S = \sqrt{\frac{\mu}{\rho}}, \tag{18}$$

in which μ and ρ are shear modulus and mass density, respectively. The mass density is defined as the mass per unit volume, which can be assumed as stationary in investigated time scales. Then, the S-wave velocity change can be expressed as

$$\frac{V_S^{\text{after}}}{V_S^{\text{before}}} = \frac{\sqrt{\mu^{\text{after}}}}{\sqrt{\mu^{\text{before}}}}. \tag{19}$$

Hence, the cause of the observed phenomenon is a temporal change in the shear modulus of near-surface layers (see additional Text S3 and Figure S28 in Supporting Information S1). It may be related to structural changes caused by Flow Liquefaction, Cyclic Mobility, and Slow Dynamics (one or a combination of more from the listed phenomena). Further, by substituting the shear modulus ratio in Equation 19 for the S-wave velocity ratio in Equation 16, we obtain the relationship from Midorikawa and Miura (2008), which is used for the estimation of the shear modulus ratio and strain during the nonlinear site response. Hence, our formulation is consistent with previous studies on the nonlinear site response.

6. Modeling

6.1. Site Response

The relation between frequencies of observed H/V peaks and theoretical SH-wave resonances (i.e., 1D site response) is discussed in the physical interpretation section. As a validation, we provide here a comparison of empirical H/V peaks and synthetic SH-wave amplification at selected sites from the Noto Peninsula region.

21699356, 2025, 4, Downloaded from https://agupubs.onlinelibrary.wiley.com/doi/10.1029/2024JB029961 by Cochrane Japan, Wiley Online Library on [03/06/2025]. See the Terms and Conditions (https://onlinelibrary.wiley.com/terms-and-conditions) on Wiley Online Library for rules of use; OA articles are governed by the applicable Creative Commons License

Considering *SH*-waves propagating through horizontally stratified viscoelastic media, the theoretical site response can be simplified as the solution to the 1D wave equation and expressed by a *SH*-wave transfer function (e.g., Kramer, 1996). The modeled transfer function expresses the ratio between Fourier spectra expected on the ground surface and the seismological bedrock outcrop (surface/outcrop transfer function). Further, to consider the scattering effect of medium heterogeneities, we also calculate the *SH*-wave stochastic model (Hallo et al., 2022, 2024; surface/outcrop stochastic model), which simulates the multipath propagation of short-period body waves. Another conducted site-response modeling approach utilizes the QWL velocity impedance contrast (Poggi et al., 2012). Because all utilized methods need a precise 1D velocity model, we performed the modeling at KiK-net sites that have available 1D velocity models down to the depth of borehole sensors. Note, that the borehole records are not used in this particular analysis, we just take advantage of velocity models. For lithological layers located deeper, seismic velocities were extracted from the Japan Integrated Velocity Structure Model (Koketsu et al., 2009, 2012). Then, the mass densities are assigned based on the empirical formula by Nagashima and Kawase (2021), and quality factors of *S*-waves are approximated to be one-tenth of the *S*-wave velocity in m/s (Olsen et al., 2003). Final composite velocity models span from the ground surface to a depth of the rigid seismological bedrock with $V_S > 3$ km/s that is reached at depths of 204–1,018 m (see velocity models in Figure 11 and Figure S29 in Supporting Information S1).

The comparison of empirical H/V spectral ratios and amplification of synthetic *SH*-wave transfer functions is shown in Figure 11 (center and right panels). Despite variations in amplitudes, frequencies of spectral peaks (colored curves) match well with frequencies of H/V peaks (black and gray curves). The best fit seems to be achieved by using the *SH*-wave stochastic model (orange curves) and the QWL velocity impedance contrast approach (yellow curves). Note, that we do not tune subsurface model velocities to improve the fit between synthetic and observed peaks; hence, the fit is as good as achieved by the original 1D composite models. This means that 1D velocity profiles are fine and that observed frequencies of earthquake H/V spectral peaks are approximately the same as those of theoretical 1D site response.

6.2. Multilayer Stratification

The formulation in Equations 15–17 expresses the relation for a single sedimentary layer on a rigid rock, while the real near-surface stratigraphy has a rather multilayer structure. Also, the observed higher resonance frequencies usually originate from a multilayer stratification. Hence, we investigate here the effect of the *S*-wave velocity change in the multilayer structure by using numerical modeling.

In this modeling test, we took the layered velocity model for the ISKH01 site (see Figure 11) as a reference model and systematically perturbed its *S*-wave velocities. The perturbed layered velocity models were subsequently used for the calculation of the surface-to-outcrop amplification by the *SH*-wave transfer function (e.g., Kramer, 1996) and the stochastic model approach (Hallo et al., 2024). The effects of the *S*-wave velocity change on the site response are shown in Figure 12. First, as predicted theoretically by Equation 16, the effect of an *S*-wave velocity drop is a decrease in the frequencies of resonance peaks (clearly visible at the whole frequency range in all tests). Note, that very strong velocity drops (stronger than −60%) cause values of the high-frequency amplification below one (dark blue colors), which can cause a temporal disappearance of high-frequency *S*-waves that was empirically observed at sites with a strongly nonstationary behavior (i.e., Figure 8). Further, frequencies of synthetic resonance peaks truly follow the theoretical relation expressed by Equation 16 if the *S*-wave velocity is perturbed jointly in all layers (see black dashed lines in Figures 12a and 12b). Nevertheless, the latter condition is usually violated as the largest change is expected in the uppermost strongly shaking units. Then, if the *S*-wave velocity changes in the uppermost two layers only, the change in amplification pattern is rather complex (Figures 12c and 12d). Still, the change predicted by Equation 16 is always less steep than the amplification pattern change modeled in the multilayer structure; which means that the prediction by Equation 16 may be used as a conservative estimate (i.e., lower threshold) of the *S*-wave velocity change. In our particular case, the retrieved short-lasting extreme frequency drops δf_l^* (Table 2) indicate extreme *S*-wave velocity drops in near-surface layers equal to or stronger than −93% to −71%.

7. Conclusions

We performed an extensive and systematic analysis of Horizontal-to-Vertical (H/V) spectral ratios from 29,140 earthquake waveforms recorded at 160 sites in the Noto Peninsula region. The identified H/V spectral peaks

21699356, 2025, 4, Downloaded from https://agupubs.onlinelibrary.wiley.com/doi/10.1029/2024JB029961 by Cochrane Japan, Wiley Online Library on [03/06/2025]. See the Terms and Conditions (https://onlinelibrary.wiley.com/terms-and-conditions) on Wiley Online Library for rules of use; OA articles are governed by the applicable Creative Commons License

10.1029/2024JB029961

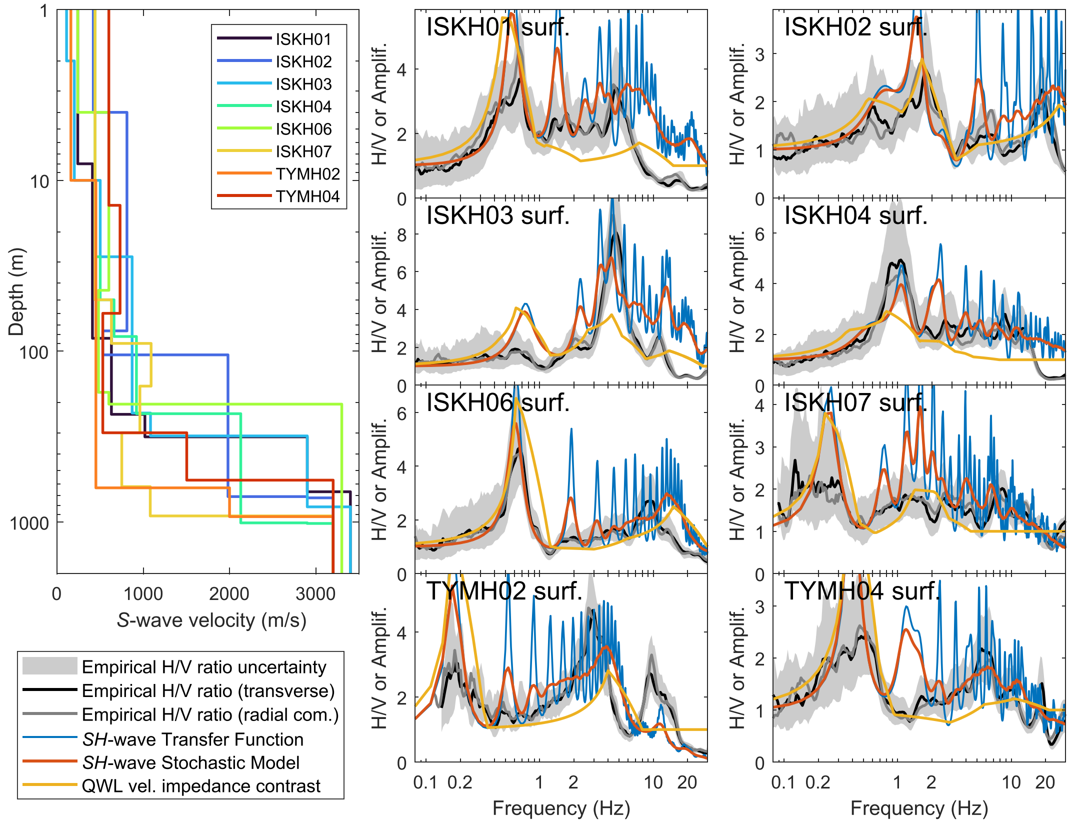

Figure 11. Site response modeling—The comparison of empirical H/V spectral ratios and *SH*-wave amplification at selected KiK-net sites. The left panel shows used *S*-wave velocity models down to the seismological bedrock with V_S > 3 km/s. The center and right panels show H/V spectral ratios observed on the ground surface (black and gray curves), surface-to-outcrop amplification of *SH*-wave transfer function (blue curves), surface-to-outcrop amplification of *SH*-wave stochastic model (orange curves), and QWL velocity impedance contrasts (yellow curves). Codes of KiK-net station are displayed in individual panels.

originate from deep lithological interfaces close to the seismological bedrock (f_l < 0.8 Hz; hundreds-to-thousands of meters) and from shallow near-surface structures ($f_l \geq 0.8$ Hz; units-to-tens of meters). The low-frequency H/V peaks exhibit significant directionality patterns in Kanazawa City and along Toyama Bay, which may be interpreted as two-dimensional resonance effects of the basin infill. The high-frequency H/V peaks show very large variability on short lateral distances.

Next, we evaluated long- and short-lasting changes in the frequency of H/V peaks at strongly shaking sites of the 2024 M_J 7.6 Noto earthquake. The long-lasting changes were determined from aftershocks occurring 0–3 days after the mainshock, and they exhibit after-to-before relative frequency drops as strong as −21%. The deep lithological layers are not significantly affected by the strong ground shaking while shallow layers are. Values of long-lasting frequency drops are correlated with observed PGV and are strongly dependent on the Joyner-Boore distance from the mainshock fault plane. We estimated, that a minimal PGV value to be able to cause a detectable long-lasting change is approximately 0.2 m/s, and a significant change can be produced if PGV >0.5 m/s. Note, that the long-lasting change may have a duration of several years, but it should be the most prominent within a few days after the mainshock.

The short-lasting coseismic changes were determined from short-period H/V spectral ratios during the 2024 M_J 7.6 Noto mainshock. Sites with clear and strong nonstationary behavior during the strong shaking are located in Anamizu Town, Wajima City, Monzen Town, Noto Town, and Noto Island. These sites also experienced significant long-lasting frequency drops. The frequency of the H/V peak decreases simultaneously with the strong shaking in all horizontal directions; and then, it recovers as a logarithmic function. This implies that the frequency

21699356, 2025, 4, Downloaded from https://agupubs.onlinelibrary.wiley.com/doi/10.1029/2024JB029961 by Cochrane Japan, Wiley Online Library on [03/06/2025]. See the Terms and Conditions (https://onlinelibrary.wiley.com/terms-and-conditions) on Wiley Online Library for rules of use; OA articles are governed by the applicable Creative Commons License

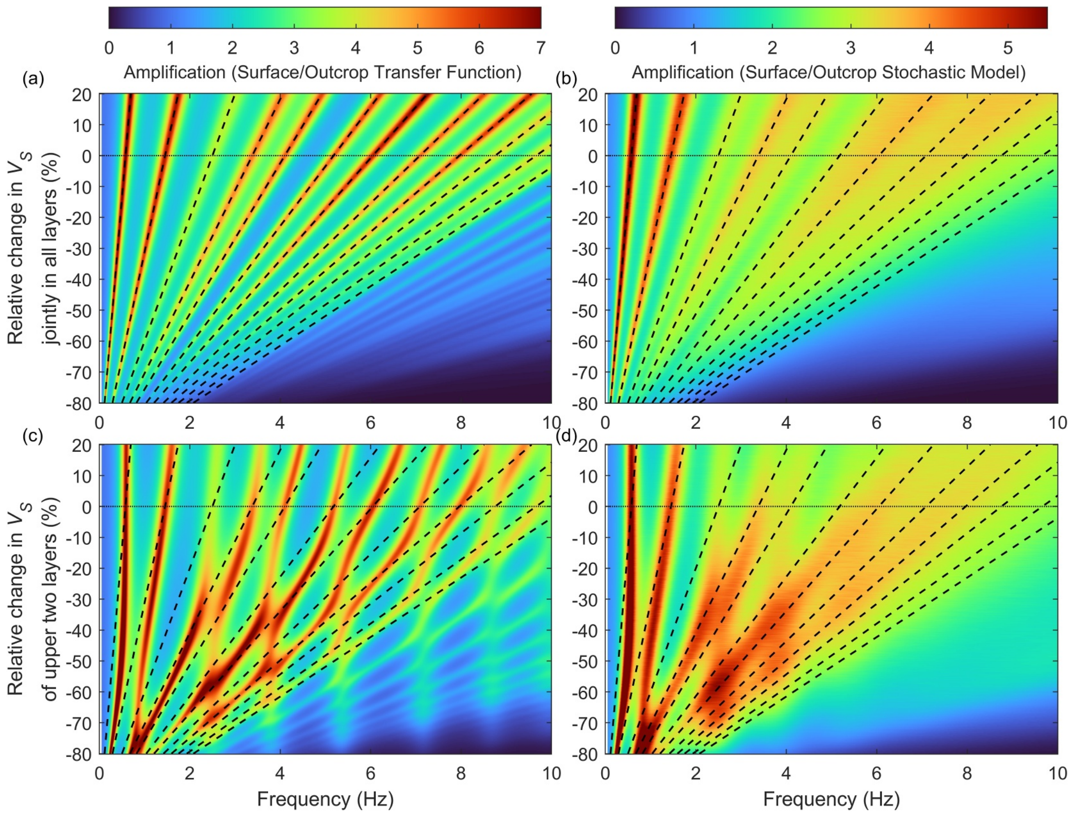

Figure 12. Site response modeling—The effects of the *S*-wave velocity change in a multilayer structure on the site response. Individual panels show the theoretical surface-to-outcrop amplification of *SH*-waves at the ISKH01 site modeled by (a), (c) transfer function and (b), (d) stochastic model (relative to an outcrop of seismological bedrock). The *S*-wave velocity is perturbed (a), (b) jointly in all layers or (c), (d) in the uppermost two layers while fixed in a deeper structure. The amplification is shown by color scale (colorbar is shared per modeling method), the amplification of the reference model is indicated by the horizontal black dotted line, and predictions by Equation 16 are shown by black dashed lines.

drop is directly related to the strong ground shaking and it is an omnidirectional phenomenon related to the transversely isotropic change in material properties. The coseismic frequency drops are much stronger than long-lasting ones. In particular, we retrieved extreme frequency drops with values from −93% to −71% (0% means no change, −100% means full liquefaction). Further, the time of the extreme frequency drop divides the nonstationary behavior into elastic softening and recovery phases, in which the softening is probably governed by the lateral force applied by cyclic shaking. The observed softening and recovery phases were fitted by a theoretical model, whose parameters may be used for earthquake scenario predictions.

The observed predominant frequency changes were physically related to drops and recovery of near-surface *S*-wave velocity as a consequence of temporal changes in the shear modulus. This was done by raising and evaluating a hypothesis based on the physical principle of standing body waves in a sedimentary layer on a rigid rock. This idealistic model is supported by numerical modeling of theoretical *SH*-wave amplification and the effects of the *S*-wave velocity change in multilayer structure. Indeed, frequencies of theoretical amplification peaks are approximately the same as frequencies of observed H/V spectral peaks, and the idealistic model is valid in a multilayer structure with some limitations as well. The temporal changes in the shear modulus during strong shaking may be caused by Flow Liquefaction, Cyclic Mobility, and Slow Dynamics phenomena.

To conclude, this paper represents a complex and unique study, and it can have a significant impact on a broad scale of geophysical research topics. For instance, the low-frequency site-response peaks with strong directionality should be considered when using specific affected stations in an earthquake source inversion to prevent misinterpretation with source effects. The coseismic and postseismic changes in the site response systematically occur at sites that experience significant PGV values, which should be considered in the earthquake-resistant

21699356, 2025, 4, Downloaded from https://agupubs.onlinelibrary.wiley.com/doi/10.1029/2024JB029961 by Cochrane Japan, Wiley Online Library on [03/06/2025]. See the Terms and Conditions (https://onlinelibrary.wiley.com/terms-and-conditions) on Wiley Online Library for rules of use; OA articles are governed by the applicable Creative Commons License

21699356, 2025, 4, Downloaded from https://agupubs.onlinelibrary.wiley.com/doi/10.1029/2024JB029961 by Cochrane Japan, Wiley Online Library on [03/06/2025]. See the Terms and Conditions (https://onlinelibrary.wiley.com/terms-and-conditions) on Wiley Online Library for rules of use; OA articles are governed by the applicable Creative Commons License

design of important buildings (e.g., by improving response spectra). Also, the nonstationary behavior during strong shaking should be considered in studies focused on the nonlinear soil response, and characteristics averaged over the whole mainshock duration should be avoided. The described phenomenon is not strictly limited to earthquakes and the Earth; hence, it is expected to be generated by other sources such as meteorite impacts on other planetary bodies, which may influence respective modeling studies.

Data Availability Statement

The waveform data underlying this article originate from various data sources as follows. The K-NET and KiK-net waveform data are available openly at the NIED strong-motion network data center (National Research Institute for Earth Science and Disaster Resilience, 2019; https://doi.org/10.17598/NIED.0004) via www.kyoshin.bosai.go.jp. The JMA Shindo-kei waveform data (Nishimae, 2004; https://www.data.jma.go.jp/eew/data/ltpgm_explain/rireki.html) are distributed by the Japan Meteorological Business Support Center on DVDs (available at http://www.jmbsc.or.jp/en/index-e.html). Ishikawa and Toyama Prefectural Shindo-kei waveform data (Nishimae, 2004) are available on demand from local governmental offices (https://www.pref.ishikawa.jp and https://www.pref.toyama.jp). The strong-motion earthquake records in Japanese ports were collected by the PARI (Nozu, 2004; https://www.pari.go.jp/en), available openly via https://www.eq.pari.go.jp/kyosin/en. The earthquake records around the Morimoto-Togashi Fault Zone were collected by the DPRI (https://sms.dpri.kyoto-u.ac.jp/e-index.html) within a research project (https://www.jishin.go.jp/database/project_report/morimoto_juten/) funded by the Ministry of Education, Culture, Sports, Science and Technology (MEXT). The JMA unified earthquake catalog (available at https://www.data.jma.go.jp/svd/eqev/data/bulletin/hypo_e.html) is produced by JMA with support from the MEXT. Next, the KiK-net 1D velocity models are available openly at the NIED strong-motion network data center www.kyoshin.bosai.go.jp. For deeper lithological layers, seismic velocities were extracted from the Japan Integrated Velocity Structure Model (Koketsu et al., 2009, 2012) available openly via https://taro.eri.u-tokyo.ac.jp/saigai/computerE.html. In addition, Supporting Information S1 includes resultant data that were used to produce figures in Tables S2–S9 in Supporting Information S1 (H/V peak frequencies, directionality, frequency change, PGA and PGV measured during the 2024 Noto earthquake), composite velocity models used for modeling purposes in Tables S10–S17 in Supporting Information S1, list of used geographical terms in Table S18 in Supporting Information S1, and photographic documentation of monitoring sites in Figures S30–S37 in Supporting Information S1. Maps were created using Generic Mapping Tools (GMT) version 6.4.0 (Wessel et al., 2019a, 2019b) licensed under the GNU Lesser General Public License (LGPL) version 3, available at https://www.generic-mapping-tools.org. In maps, the land elevation data are from the NASA SRTM 3-arc-second data set (NASA Jet Propulsion Laboratory, 2013), and ocean depth data are from Tozer et al. (2019). Plots were made using Matlab software version 2023b (MathWorks, 2023; https://www.mathworks.com) licensed under the Campus-Wide License of Kyoto University. The surface-to-outcrop transfer functions and stochastic models were computed by Matlab codes licensed under the GNU General Public License (GPL) version 3, available in the electronic supplemental material S4 of Hallo et al. (2022) via https://doi.org/10.1785/0120220038. All websites were last accessed on 15 May 2024.

Acknowledgments

We are grateful to our colleagues from the Disaster Prevention Research Institute (DPRI) of Kyoto University for their support, to Junior High and Firefighters Schools in Kanazawa and Hakusan cities for allowing the placement of seismic sensors, and to the researchers from the Geo-Research Institute for their help in fieldworks during the temporary observation around the Morimoto-Togashi Fault Zone. We also appreciate the editor Rachel Abercrombie, associate editor Nori Nakata, reviewer Fabian Bonilla, and an anonymous reviewer for their comments and suggestions. We acknowledge the National Research Institute for Earth Science and Disaster Resilience (NIED), Japan Meteorological Agency (JMA), Ishikawa and Toyama Prefectural Governments, and Port and Airport Research Institute (PARI) for operating strong-motion and intensity monitoring stations used in this study. Miroslav Hallo was supported by the Japan Society for the Promotion of Science (JSPS) through Fellowship number P23070 and Grant-in-Aid for JSPS Fellows number 23KF0149. Authors adhere to the Scientific Ethics and Research Integrity. This work was conceptualized, conducted, and written by humans without any help from artificial intelligence.

References

Aguirre, J., & Irikura, K. (1997). Nonlinearity, liquefaction, and velocity variation of soft soil layers in Port Island, Kobe, during the Hyogo-ken Nanbu earthquake. *Bulletin of the Seismological Society of America*, *87*(5), 1244–1258. https://doi.org/10.1785/BSSA0870051244

Amezawa, Y., Hiramatsu, Y., Miyakawa, A., Imanishi, K., & Otsubo, M. (2023). Long-living earthquake swarm and intermittent seismicity in the northeastern tip of the Noto Peninsula, Japan. *Geophysical Research Letters*, *50*(8), e2022GL102670. https://doi.org/10.1029/2022GL102670

Aoi, S., Asano, Y., Kunugi, T., Kimura, T., Uehira, K., Takahashi, N., et al. (2020). MOWLAS: NIED observation network for earthquake, tsunami and volcano. *Earth Planets and Space*, *72*(1), 126. https://doi.org/10.1186/s40623-020-01250-x

Arias, A. (1970). A measure of earthquake intensity. In R. J. Hansen (Ed.), *Seismic design for nuclear power plants*. Massachusetts Institute of Technology Press.

Asano, K., & Iwata, T. (2011). Source-rupture process of the 2007 Noto Hanto, Japan, earthquake estimated by the joint inversion of strong motion and GPS data. *Bulletin of the Seismological Society of America*, *101*(5), 2467–2480. https://doi.org/10.1785/0120100254

Asano, K., & Iwata, T. (2024). Source rupture process of the 2024 Noto Hanto earthquake by waveform inversion of strong motion records. *Poster presented at Japan Geoscience Union Meeting 2024 (U15-P20)*. Retrieved from https://confit.atlas.jp/guide/event/jpgu2024/subject/U15-P20/class

Asano, K., Iwata, T., Iwaki, A., Kuriyama, M., & Suzuki, W. (2009). Ground motion characteristics in Anamizu town obtained from earthquake and microtremor observations. *Journal of the Seismological Society of Japan*, *62*(2), 121–135. https://doi.org/10.4294/zisin.62.121

Asano, K., Iwata, T., Miyakoshi, K., & Ohori, M. (2015). Study on underground velocity structure model in the Kaga Plain and the Ochigata Plain using microtremor observations. *Journal of Japan Association for Earthquake Engineering*, *15*(7), 194–204. https://doi.org/10.5610/jaee.15.7_194

Asano, K., Yoshida, K., Miyakoshi, K., Ohori, M., & Iwata, T. (2020). Microtremor surveys in large sedimentary basins on the coast of the Sea of Japan. In *Proceedings of the 17th world conference on earthquake engineering (1f-0006)*. National Information Centre of Earthquake Engineering.

Assimaki, D., Li, W., Steidl, J., & Schmedes, J. (2008). Quantifying nonlinearity susceptibility via site-response modeling uncertainty at three sites in the Los Angeles Basin. *Bulletin of the Seismological Society of America*, *98*(5), 2364–2390. https://doi.org/10.1785/0120080031

Bard, P.-Y., & Bouchon, M. (1985). The two-dimensional resonance of sediment-filled valleys. *Bulletin of the Seismological Society of America*, *75*(2), 519–541. https://doi.org/10.1785/BSSA0750020519

Beresnev, I. A., & Wen, K.-L. (1996). Nonlinear soil response—A reality? *Bulletin of the Seismological Society of America*, *86*(6), 1964–1978. https://doi.org/10.1785/BSSA0860061964

Bonilla, L. F., Guéguen, P., & Ben-Zion, Y. (2019). Monitoring coseismic temporal changes of shallow material during strong ground motion with interferometry and autocorrelation. *Bulletin of the Seismological Society of America*, *109*(1), 187–198. https://doi.org/10.1785/0120180092

Bonilla, L. F., Steidl, J. H., Lindley, G. T., Tumarkin, A. G., & Archuleta, R. J. (1997). Site amplification in the San Fernando Valley, California: Variability of site-effect estimation using the *S*-wave, coda, and *H/V* methods. *Bulletin of the Seismological Society of America*, *87*(3), 710–730. https://doi.org/10.1785/BSSA0870030710

Bonnefoy-Claudet, S., Köhler, A., Cornou, C., Wathelet, M., & Bard, P.-Y. (2008). Effects of Love waves on microtremor H/V ratio. *Bulletin of the Seismological Society of America*, *98*(1), 288–300. https://doi.org/10.1785/0120070063

Borcherdt, R. D. (1970). Effects of local geology on ground motion near San Francisco Bay. *Bulletin of the Seismological Society of America*, *60*(1), 29–61. https://doi.org/10.1785/BSSA0600010029

Castro, G. (1975). Liquefaction and cyclic mobility of saturated sands. *Journal of Geotechnical and Geoenvironmental Engineering*, *101*(6), 551–569. https://doi.org/10.1061/AJGEB6.0000173

Esfahani, R., Cotton, F., & Bonilla, L. F. (2024). Temporal variations of the "in situ" nonlinear behaviour of shallow sediments during the 2016 Kumamoto Earthquake sequence. *Geophysical Journal International*, *238*(3), 1626–1637. https://doi.org/10.1093/gji/ggae222

Fäh, D., Kind, F., & Giardini, D. (2001). A theoretical investigation of average H/V ratios. *Geophysical Journal International*, *145*(2), 535–549. https://doi.org/10.1046/j.0956-540x.2001.01406.x

Faraday, M. (1831). On a peculiar class of acoustical figures; and on certain forms assumed by groups of particles upon vibrating elastic surfaces. *Philosophical Transactions of the Royal Society*, *121*, 299–340. https://doi.org/10.1098/rstl.1831.0018

Fujii, Y., & Satake, K. (2024). Slip distribution of the 2024 Noto Peninsula earthquake (M_{JMA} 7.6) estimated from tsunami waveforms and GNSS data. *Earth Planets and Space*, *76*(1), 44. https://doi.org/10.1186/s40623-024-01991-z

Gröchenig, K. (2001). *Foundations of time-frequency analysis*. Birkhäuser.

Guyer, R. A., McCall, K. R., & Van Den Abeele, K. (1998). Slow elastic dynamics in a resonant bar of rock. *Geophysical Research Letters*, *25*(10), 1585–1588. https://doi.org/10.1029/98GL51231

Hallo, M., Bergamo, P., & Fäh, D. (2022). Stochastic model to characterize high-frequency ground motion at depth validated by KiK-net vertical array data. *Bulletin of the Seismological Society of America*, *112*(4), 1997–2017. https://doi.org/10.1785/0120220038

Hallo, M., Bergamo, P., & Fäh, D. (2024). Multipath transfer-function correction method to predict site-specific amplification at city scale. *Seismological Research Letters*, *95*(1), 172–185. https://doi.org/10.1785/0220230213

Hill, D. P., Reasenberg, P. A., Michael, A., Arabaz, W. J., Beroza, G., Brumbaugh, D., et al. (1993). Seismicity remotely triggered by the magnitude 7.3 Landers, California, earthquake. *Science*, *260*(5114), 1617–1623. https://doi.org/10.1126/science.260.5114.1617

Hobiger, M., Bard, P.-Y., Cornou, C., & Le Bihan, N. (2009). Single station determination of Rayleigh wave ellipticity by using the random decrement technique (RayDec). *Geophysical Research Letters*, *36*(14), L14303. https://doi.org/10.1029/2009GL038863

Iai, S., Morita, T., Kameoka, T., Matsunaga, Y., & Abiko, K. (1995). Response of a dense sand deposit during 1993 Kushiro-Oki earthquake. *Soils and Foundations*, *35*(1), 115–131. https://doi.org/10.3208/sandf1972.35.115

Ibs-von Seht, M., & Wohlenberg, J. (1999). Microtremor measurements used to map thickness of soft sediments. *Bulletin of the Seismological Society of America*, *89*(1), 250–259. https://doi.org/10.1785/BSSA0890010250

Iwata, T., Asano, K., Kuriyama, M., & Iwaki, A. (2008). Non-linear site response characteristics of K-NET ISK005 station and relation to the earthquake disaster during the 2007 Noto-Hanto earthquake, central Japan. In *Proceedings of the 14th world conference on earthquake engineering (01-1026). Beijing, China: International association for earthquake engineering*.

Joyner, W. B., & Boore, D. M. (1981). Peak horizontal acceleration and velocity from strong-motion records including records from the 1979 Imperial Valley, California, earthquake. *Bulletin of the Seismological Society of America*, *71*(6), 2011–2038. https://doi.org/10.1785/BSSA0710062011

Joyner, W. B., Warrick, R. E., & Fumal, T. E. (1981). The effect of quaternary alluvium on strong ground motion in the Coyote Lake, California, earthquake of 1979. *Bulletin of the Seismological Society of America*, *71*(4), 1333–1349. https://doi.org/10.1785/BSSA0710041333

Kato, A. (2024). Implications of fault-valve behavior from immediate aftershocks following the 2023 M_j6.5 earthquake beneath the Noto Peninsula Central Japan. *Geophysical Research Letters*, *51*(1), e2023GL106444. https://doi.org/10.1029/2023GL106444

Kawase, H., Mori, Y., & Nagashima, F. (2018). Difference of horizontal-to-vertical spectral ratios of observed earthquakes and microtremors and its application to S-wave velocity inversion based on the diffuse field concept. *Earth Planets and Space*, *70*, 1. https://doi.org/10.1186/s40623-017-0766-4

Kawase, H., Satoh, T., Fukutake, K., & Irikura, K. (1995). Borehole records observed at the port Island in Kobe during the Hyogoken Nanbu earthquake of 1995 and its simulation. *Journal of Structural and Construction Engineering (Transactions of Architectural Institute of Japan)*, *60*(475), 83–92. https://doi.org/10.3130/aijs.60.83_2

Koketsu, K., Miyake, H., & Suzuki, H. (2012). Japan integrated velocity structure model version 1. In *Proceedings of the 15th world conference on earthquake engineering (10463)*. Sociedade Portuguesa de Engenharia Sismica.

Koketsu, K., Miyake, H., & Tanaka, Y. (2009). A proposal for a standard procedure of modeling 3-D velocity structures and its application to the Tokyo metropolitan area, Japan. *Tectonophysics*, *472*(1–4), 290–300. https://doi.org/10.1016/j.tecto.2008.05.037

Konno, K., & Ohmachi, T. (1998). Ground-motion characteristics estimated from spectral ratio between horizontal and vertical components of microtremor. *Bulletin of the Seismological Society of America*, *88*(1), 228–241. https://doi.org/10.1785/BSSA0880010228

Kramer, S. L. (1996). *Geotechnical earthquake engineering*. Prentice Hall.

Kurahashi, S., Masaki, K., & Irikura, K. (2008). Source model of the 2007 Noto-Hanto earthquake (M_w 6.7) for estimating broad-band strong ground motion. *Earth Planets and Space*, *60*(2), 89–94. https://doi.org/10.1186/BF03352766

Lermo, J., & Chávez-García, F. J. (1993). Site effect evaluation using spectral ratios with only one station. *Bulletin of the Seismological Society of America*, *83*(5), 1574–1594. https://doi.org/10.1785/BSSA0830051574

Li, Y. G., Vidale, J. E., Aki, K., Xu, F., & Burdette, T. (1998). Evidence of shallow fault zone strengthening after the 1992 *M*7.5 Landers, California, earthquake. *Science*, *279*(5348), 217–219. https://doi.org/10.1126/science.279.5348.217

21699356, 2025, 4, Downloaded from https://agupubs.onlinelibrary.wiley.com/doi/10.1029/2024JB029961 by Cochrane Japan, Wiley Online Library on [03/06/2025]. See the Terms and Conditions (https://onlinelibrary.wiley.com/terms-and-conditions) on Wiley Online Library for rules of use; OA articles are governed by the applicable Creative Commons License

Maranò, S., Reller, C., Loeliger, H.-A., & Fäh, D. (2012). Seismic waves estimation and wavefield decomposition: Application to ambient vibrations. *Geophysical Journal International*, *191*(1), 175–188. https://doi.org/10.1111/j.1365-246X.2012.05593.x

MathWorks. (2023). MATLAB version 23.2.0.2409890 (R2023b), update 3 [Software]. *The MathWorks, Inc*. https://www.mathworks.com/products/matlab.html

Matsushima, S., Kosaka, H., & Kawase, H. (2017). Directionally dependent horizontal-to-vertical spectral ratios of microtremors at Onahama, Fukushima, Japan. *Earth Planets and Space*, *69*(1), 96. https://doi.org/10.1186/s40623-017-0680-9

Midorikawa, S., & Miura, H. (2008). Nonlinear behavior of soil response observed in strong-motion records from recent Japanese earthquakes. In *Proceedings of the 14th world conference on earthquake engineering (02-0017). Beijing, China: International association for earthquake engineering*.

Ministry of Land, Infrastructure, Transport and Tourism. (2013). Liquefaction susceptibility map for Ishikawa Prefecture: 石川県内液状化しやすさマップ. Hokuriku regional development bureau of the Ministry of land, infrastructure, Transport and Tourism (MLIT). *Hokuriku Branch of the Japanese Geotechnical Society (JGS)*. Retrieved from https://www.hrr.mlit.go.jp/ekijoka/attention.html

Nagase, H., & Ishihara, K. (1988). Liquefaction-induced compaction and settlement of sand during earthquakes. *Soils and Foundations*, *28*(1), 65–76. https://doi.org/10.3208/sandf1972.28.65

Nagashima, F., & Kawase, H. (2021). The relationship between Vs, Vp, density and depth based on PS-logging data at K-NET and KiK-net sites. *Geophysical Journal International*, *225*(3), 1467–1491. https://doi.org/10.1093/gji/ggab037

Nakajima, J. (2022). Crustal structure beneath earthquake swarm in the Noto peninsula, Japan. *Earth Planets and Space*, *74*(1), 160. https://doi.org/10.1186/s40623-022-01719-x

Nakamura, Y. (1989). A method for dynamic characteristics estimation of subsurface using microtremor on the ground surface. *Quarterly Report of Railway Technical Research Institute*, *30*(1), 25–33.

Nakamura, Y. (2000). Clear identification of fundamental idea of Nakamura's technique and its applications. In *Proceedings of the 12th world conference on earthquake engineering* (Vol. 2656). New Zealand Society for Earthquake Engineering.

NASA Jet Propulsion Laboratory. (2013). NASA shuttle radar topography mission global 3 arc second [Dataset]. *NASA Land Processes Distributed Active Archive Center*. https://doi.org/10.5067/MEaSUREs/SRTM/SRTMGL3.003

National Research Institute for Earth Science and Disaster Resilience. (2019). NIED K-NET, KiK-net [Dataset]. *National Research Institute for Earth Science and Disaster Resilience*. https://doi.org/10.17598/NIED.0004

Nishimae, Y. (2004). Observation of seismic intensity and strong ground motion by Japan Meteorological Agency and local governments in Japan. *Journal of Japan Association for Earthquake Engineering*, *4*(3), 75–78. https://doi.org/10.5610/jaee.4.3_75

Nishimura, T., Hiramatsu, Y., & Ohta, Y. (2023). Episodic transient deformation revealed by the analysis of multiple GNSS networks in the Noto Peninsula, central Japan. *Scientific Reports*, *13*(1), 8381. https://doi.org/10.1038/s41598-023-35459-z

Nogoshi, M., & Igarashi, T. (1971). On the amplitude characteristics of microtremor (part 2). *Journal of the Seismological Society of Japan*, *24*(1), 26–40. https://doi.org/10.4294/zisin1948.24.1_26

Nozu, A. (2004). Current status of strong-motion earthquake observation in Japanese ports. *Journal of Japan Association for Earthquake Engineering*, *4*(3), 79–83. https://doi.org/10.5610/jaee.4.3_79

Ohmi, S., Hirahara, K., Wada, H., & Ito, K. (2008). Temporal variations of crustal structure in the source region of the 2007 Noto Hanto Earthquake, central Japan, with passive image interferometry. *Earth Planets and Space*, *60*(10), 1069–1074. https://doi.org/10.1186/BF03352871

Okubo, K., Delbridge, B. G., & Denolle, M. A. (2024). Monitoring velocity change over 20 years at Parkfield. *Journal of Geophysical Research: Solid Earth*, *129*(4), e2023JB028084. https://doi.org/10.1029/2023JB028084

Olsen, K. B., Day, S. M., & Bradley, C. R. (2003). Estimation of Q for long-period (>2 sec) waves in the Los Angeles basin. *Bulletin of the Seismological Society of America*, *93*(2), 627–638. https://doi.org/10.1785/0120020135

Ostrovsky, L., Lebedev, A., Riviere, J., Shokouhi, P., Wu, C., Stuber Geesey, M. A., & Johnson, P. A. (2019). Long-time relaxation induced by dynamic forcing in geomaterials. *Journal of Geophysical Research: Solid Earth*, *124*(5), 5003–5013. https://doi.org/10.1029/2018JB017076

Parolai, S., Richwalski, S. M., Milkereit, C., & Bormann, P. (2004). Assessment of the stability of H/V spectral ratios from ambient noise and comparison with earthquake data in the Cologne area (Germany). *Tectonophysics*, *390*(1–4), 57–73. https://doi.org/10.1016/j.tecto.2004.03.024

Pavlenko, O. V., & Irikura, K. (2006). Nonlinear behavior of soils revealed from the records of the 2000 Tottori, Japan, earthquake at stations of the digital strong-motion network Kik-net. *Bulletin of the Seismological Society of America*, *96*(6), 2131–2145. https://doi.org/10.1785/0120060069

Poggi, V., Edwards, B., & Fäh, D. (2012). Characterizing the Vertical-to-Horizontal ratio of ground motion at soft-sediment sites. *Bulletin of the Seismological Society of America*, *102*(6), 2741–2756. https://doi.org/10.1785/0120120039

Régnier, J., Cadet, H., Bonilla, L. F., Bertrand, E., & Semblat, J.-F. (2013). Assessing nonlinear behavior of soils in seismic site response: Statistical analysis on KiK-net strong-motion data. *Bulletin of the Seismological Society of America*, *103*(3), 1750–1770. https://doi.org/10.1785/0120120240

Roten, D., Fäh, D., Cornou, C., & Giardini, D. (2006). Two-dimensional resonances in Alpine valleys identified from ambient vibration wavefields. *Geophysical Journal International*, *165*(3), 889–905. https://doi.org/10.1111/j.1365-246X.2006.02935.x

Rubinstein, J. L., Uchida, N., & Beroza, G. C. (2007). Seismic velocity reductions caused by the 2003 Tokachi-Oki earthquake. *Journal of Geophysical Research*, *112*(B5), B05315. https://doi.org/10.1029/2006JB004440

Sakai, S., Kato, A., Iidaka, T., Iwasaki, T., Kurashimo, E., Igarashi, T., et al. (2008). Highly resolved distribution of aftershocks of the 2007 Noto Hanto Earthquake by a dense seismic observation. *Earth Planets and Space*, *60*(2), 83–88. https://doi.org/10.1186/BF03352765

Sánchez-Sesma, F. J., Rodríguez, M., Iturrarán-Viveros, U., Luzón, F., Campillo, M., Margerin, L., et al. (2011). A theory for microtremor H/V spectral ratio: Application for a layered medium. *Geophysical Journal International*, *186*(1), 221–225. https://doi.org/10.1111/j.1365-246X.2011.05064.x

Sato, K., Kokusho, T., Matsumoto, M., & Yamada, E. (1996). Nonlinear seismic response and soil property during strong motion. *Soils and Foundations*, *36*(Special), 41–52. https://doi.org/10.3208/sandf.36.Special_41

Sawazaki, K., Sato, H., Nakahara, H., & Nishimura, T. (2006). Temporal change in site response caused by earthquake strong motion as revealed from coda spectral ratio measurement. *Geophysical Research Letters*, *33*(21), L21303. https://doi.org/10.1029/2006GL027938

Sawazaki, K., Sato, H., Nakahara, H., & Nishimura, T. (2009). Time-lapse changes of seismic velocity in the shallow ground caused by strong ground motion shock of the 2000 Western-Tottori earthquake, Japan, as Revealed from coda deconvolution analysis. *Bulletin of the Seismological Society of America*, *99*(1), 352–366. https://doi.org/10.1785/0120080058

Scalerandi, M., Gliozzi, A. S., Bruno, C. L. E., & Antonaci, P. (2010). Nonequilibrium and hysteresis in solids: Disentangling conditioning from nonlinear elasticity. *Physical Review B*, *81*(10), 104114. https://doi.org/10.1103/PhysRevB.81.104114

21699356, 2025, 4, Downloaded from https://agupubs.onlinelibrary.wiley.com/doi/10.1029/2024JB029961 by Cochrane Japan, Wiley Online Library on [03/06/2025]. See the Terms and Conditions (https://onlinelibrary.wiley.com/terms-and-conditions) on Wiley Online Library for rules of use; OA articles are governed by the applicable Creative Commons License

Schaff, D. P., & Beroza, G. C. (2004). Coseismic and postseismic velocity changes measured by repeating earthquakes. *Journal of Geophysical Research*, *109*(B10), B10302. https://doi.org/10.1029/2004JB003011

Seed, H. B., & Idriss, I. M. (1967). Analysis of soil liquefaction: Niigata earthquake. *Journal of the Soil Mechanics and Foundations Division*, *93*(3), 83–108. https://doi.org/10.1061/JSFEAQ.0000981

Shokouhi, P., Rivière, J., Guyer, R. A., & Johnson, P. A. (2017). Slow dynamics of consolidated granular systems: Multi-scale relaxation. *Applied Physics Letters*, *111*(25), 251604. https://doi.org/10.1063/1.5010043

TenCate, J. A., & Shankland, T. J. (1996). Slow dynamics in the nonlinear elastic response of Berea sandstone. *Geophysical Research Letters*, *23*(21), 3019–3022. https://doi.org/10.1029/96GL02884

TenCate, J. A., Smith, E., & Guyer, R. A. (2000). Universal slow dynamics in granular solids. *Physical Review Letters*, *85*(5), 1020–1023. https://doi.org/10.1103/PhysRevLett.85.1020

Terakawa, T., & Matsu'ura, M. (2010). The 3-D tectonic stress fields in and around Japan inverted from centroid moment tensor data of seismic events. *Tectonics*, *29*(6), TC6008. https://doi.org/10.1029/2009TC002626

Tozer, B., Sandwell, D. T., Smith, W. H. F., Olson, C., Beale, J. R., & Wessel, P. (2019). Global bathymetry and topography at 15 arc sec: SRTM15+ [Dataset]. *OpenTopography*. https://doi.org/10.5069/G92R3PT9

Vassallo, M., Cultrera, G., Di Giulio, G., Cara, F., & Milana, G. (2022). Peak frequency changes from HV spectral ratios in Central Italy: Effects of strong motions and seasonality over 12 years of observations. *Journal of Geophysical Research: Solid Earth*, *127*(5), e2021JB023848. https://doi.org/10.1029/2021JB023848

Viens, L., & Delbridge, B. G. (2024). Shallow soil response to a buried chemical explosion with geophones and distributed acoustic sensing. *Journal of Geophysical Research: Solid Earth*, *129*(7), e2023JB028416. https://doi.org/10.1029/2023JB028416

Wen, K.-L., Chang, T.-M., Lin, C.-M., & Chiang, H.-J. (2006). Identification of nonlinear site response using the H/V spectral ratio method. *Terrestrial, Atmospheric and Oceanic Sciences*, *17*(3), 533–546. https://doi.org/10.3319/TAO.2006.17.3.533(T)

Wessel, P., Luis, J. F., Uieda, L., Scharroo, R., Wobbe, F., Smith, W. H. F., & Tian, D. (2019a). The generic mapping tools version 6. *Geochemistry, Geophysics, Geosystems*, *20*(11), 5556–5564. https://doi.org/10.1029/2019gc008515

Wessel, P., Luis, J. F., Uieda, L., Scharroo, R., Wobbe, F., Smith, W. H. F., & Tian, D. (2019b). The generic mapping tools version 6 [Software]. *Zenodo*. https://doi.org/10.5281/zenodo.3407866

Wu, C., & Peng, Z. (2011). Temporal changes of site response during the 2011 M_w 9.0 off the Pacific coast of Tohoku Earthquake. *Earth Planets and Space*, *63*(7), 51–795. https://doi.org/10.5047/eps.2011.06.011

Wu, C., & Peng, Z. (2012). Long-term change of site response after the M_W 9.0 Tohoku earthquake in Japan. *Earth Planets and Space*, *64*(12), 1259–1266. https://doi.org/10.5047/eps.2012.05.012

Yoshida, K., Uno, M., Matsuzawa, T., Yukutake, Y., Mukuhira, Y., Sato, H., & Yoshida, T. (2023). Upward earthquake swarm migration in the northeastern Noto Peninsula, Japan, initiated from a deep ring-shaped cluster: Possibility of fluid leakage from a hidden magma system. *Journal of Geophysical Research: Solid Earth*, *128*(6), e2022JB026047. https://doi.org/10.1029/2022jb026047

Yoshimi, M., & Yoshida, K. (2008). Site amplification and strong ground motion of the 2007 Noto Hanto, Japan, earthquake estimated from aftershock observation. *Earth Planets and Space*, *60*(3), 161–167. https://doi.org/10.1186/BF03352779

21699356, 2025, 4, Downloaded from https://agupubs.onlinelibrary.wiley.com/doi/10.1029/2024JB029961 by Cochrane Japan, Wiley Online Library on [03/06/2025]. See the Terms and Conditions (https://onlinelibrary.wiley.com/terms-and-conditions) on Wiley Online Library for rules of use; OA articles are governed by the applicable Creative Commons License